Chapter 4

Effect of Photonic Structures in Organic Light-Emitting Diodes – Light Extraction and Polarization Characteristics

Soon Moon Jeong and Hideo Takezoe

Additional information is available at the end of the chapter

http://dx.doi.org/10.5772/54669

1. Introduction

The development in organic light emitting diodes (OLEDs) has been one of the fastest growing research areas because of their potential applications in lighting and flat panel displays. Some commercialization of OLED devices such as lightings and displays has already been made. In particular, OLED displays are awaiting true commercialization toward large market. However, there are still several problems to be solved. Particularly two areas require ongoing improvements, 1) light extraction and 2) polarization. In this chapter the research activities in these two areas are summarized.

2. Light extraction

As far as the material for organic light-emitting diodes (OLEDs) is concerned, semiconductor-based organic light emitters are the obvious choice because semiconducting organic light-emitting materials have reached a high level with internal quantum efficiencies of ~100% [1]. Unfortunately, however, most of this light is trapped inside OLEDs, and only 20% can be outcoupled because of the total internal reflection [2-7]. In this section, various light extraction technologies are reviewed to suppress guided light loss. In particular, the enhanced light extraction efficiency by means of photonic structures onto OLEDs is discussed in depth.

2.1. Limited light extraction and improvement strategy

OLEDs suffer from poor external efficiency that arises from Snell's law; i.e., light generated in a high-refractive-index layer tends to remain trapped in the layer due to total internal reflection [2,3]. In fact, whatever the internal quantum efficiency might be, the light

extraction efficiency of OLEDs with flat multi-layered structures including no additional surface modifications is typically only about 20% of the internal quantum efficiency [4,5]. In such OLEDs, the extracted emission cone to air is very small and only a small fraction of the light generated in the material can be outcoupled from the device but the rest is trapped within by the total internal reflection. The emitted light has to travel from the emissive layer ($n_{organic}$ = 1.6~1.7) through the ITO contact (n_{ITO} = 1.8~2.0) and the glass substrate ($n_{substrate}$ = ~1.5) and finally into air (n_{air} = 1). By using ray optics, simply the amount of extracted light out of incident light to the air η can be estimated by the following relation [8].

$$\eta = \frac{1}{2n^2} \tag{1}$$

where n is the effective refractive index of the emissive layer with respect to the that of outcoupled space (air) By taking account of Fresnel reflections at the glass/air interface [9] the calculated extraction of light to the air is only about ~17%.

Resumption of at least part of the remaining trapped light (~80%) has been one of the most important issues in fabricating OLEDs for practical applications over the past years. The intense research efforts have been focused on, e.g., substrate surface roughening [10], microlenses [11,12], monolayer of silica spheres as a scattering medium [13], insertion of low-refractive-index materials [5], distributed Bragg reflectors (DBRs) [14-20], and one-dimensional (1-D) or two-dimensional (2-D) photonic structures [21-28]. The research developments in these areas are described below:

Light extraction by scattering: One of the low-cost methods for enhanced light extraction efficiency is roughening the substrate surface as shown in Fig. 1(a). The roughness causes random light scattering at the interface between substrate and air, and thus a guided light can be extracted from OLEDs. Schnitzer *et al*. have demonstrated a 30% increase of external efficiency in GaAs light-emitting diodes (LEDs) using nanotextured surface [29]. In case of OLEDs, however, this surface roughening techniques have not been used widely because semiconducting organic materials have relatively low refractive index of 1.7 compared with inorganic materials (n=3.5). Although a randomly rusted surface can extract guided modes, it also interrupts the external air modes (within critical angle) by non-transparent surface. Therefore, inorganic LEDs with larger amount of guided modes have better extraction ratio than organic LEDs.

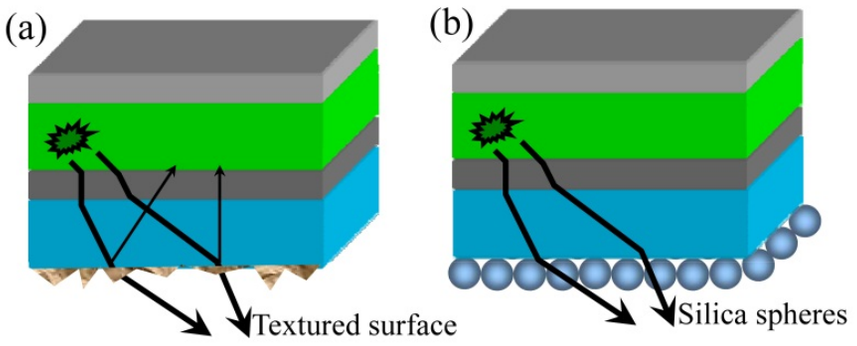

Figure 1. Schematic structure of OLEDs with modified substrate surface and light extraction.

To overcome this problem, an ordered monolayer of silica microspheres with a diameter 550 nm as a scattering medium has been used by Yamasaki *et al.* as shown in Fig. 1(b) [13]. They have used hexagonally closed packed silica microspheres to enhance the light extraction by a 2-D diffraction lattice. However, in this structure a spectral change is inevitable by the periodic configuration of microspheres, and the device does not show Lambertian emission with the increase of output polar angle from 0° to 90°.

Microlens array: Figure 2 shows a microlens that has been used as an array for light extraction from the substrate modes [11,12]. The range of diameter of the semi-spherical lens is typically from a few μm to hundreds of μm. Without such lenses, light emitted into substrate with large incidence angles is totally reflected internally by the flat interface between the substrate and air. However, by introducing semi-spherical lenses, the considerable degree of light is transmitted to the air with less total internal reflection because the incidence angle with respect to the surface normal of the lens is now lower than the critical angle. Recently this technology has mostly been used in OLEDs fabricated for lighting because low-cost fabrication of light extraction films is possible via imprint processes. However, the enhanced light extraction efficiency achieved so far is only 1.5-1.7 times of that of reference devices without lenses. To make the matter worse, the color variation with increase of angle is inevitable, preventing the Lambertian emission which is very essential for lighting. It is shown by Lim *et al*. that randomly fabricated microlenses can solve this problem to a certain extent and improve the angle dependence [30].

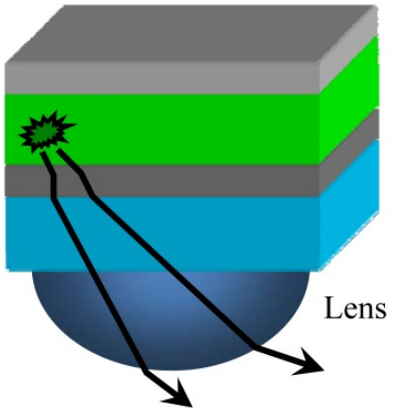

Figure 2. Schematic structure of OLEDs with a microlens and light extraction.

Insertion of low-refractive-index materials: Tsutsui *et al*. [5] have used ultrathin organic emissive layers as very poor waveguides with only a very few allowed modes. This allows a considerable amount of light to leak into the substrate, and eq. (1) is no longer valid. In addition, if the index of refraction of the substrate can also be lowered, the light output can be improved significantly as shown in Fig. 3. Tsutsui *et al*. have proposed the use of aerogels with a refractive index close to that of air ($n_{aerogel}$~1) and demonstrated that the out-coupling efficiency gets doubled.

Distributed Bragg reflectors (Microcavity): Another promising light extraction technique is the use of microcavity structures [18-20,31,32]. In microcavity devices, the internal emission can

be effectively extracted via interference effects. In addition, microcavity provides us with spectral narrowing and spatial redistribution of the emission. Microcavity using inorganic distributed Bragg reflectors (DBRs) consisting of alternating inorganic layers with different refractive indices has been extensively studied over the past several decades. The advantage of DBRs is that they may have very high reflectivity and very low loss. These reflectors have a selective reflectivity in a specific wavelength range, which can form constructive interference, and effectively suppress other modes and induce a high reflectance over a certain range of wavelengths depending on the difference in refractive indices of constituting layers. This leads to spectral narrowing and intensity enhancement of spontaneous emission in microcavity OLEDs.

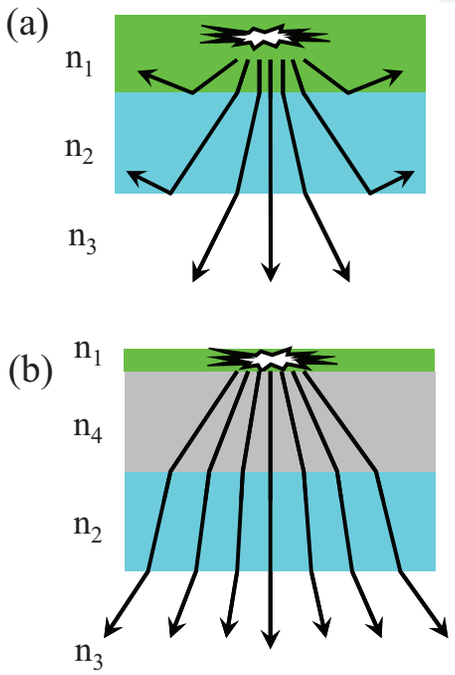

Figure 3. Schematic diagram of light extraction from OLED with (a) conventional structure and (b) structure with a thin active layer and a low-refractive index layer.[5] Copyright 2001, Wiley-VCH.

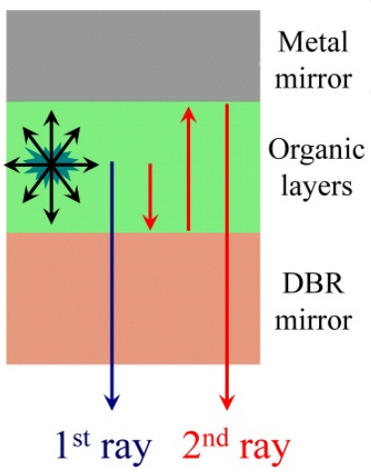

Figure 4. Schematic structure of microcavity OLEDs.

The schematic structure of a microcavity is shown in Fig. 4. The total optical path difference between direct emission and emission after single-round reflection L (see Fig. 4) is given by:

$$L = \frac{\lambda}{2}\left(\frac{n_{eff}}{\Delta n}\right) + \sum_i n_i L_i + \left|\frac{\phi_m}{4\pi}\lambda\right| \tag{2}$$

where n_{eff} is the effective refractive index, n_i is refractive index of ith layer, φ_m denotes phase shift. The first, second, and third terms stand for effective penetration depth, summation of the optical thickness in each layer, and phase shift, respectively. Usually, the total thickness of the organic materials in OLED structure is about 100 nm and the ITO thickness is determined by considering good electrical conductance and high transparence. Therefore, the optical length of the cavity can be modified by varying the second term in eq. (2). If resonant condition for constructive interference is $2L=m\lambda$, the light with λ is selectively enhanced and the color purity is also enhanced.

Diffractive resonators: The application of Bragg grating to OLEDs has been reported by Matterson *et al*. [21] and Lupton *et al*. [22]. They have demonstrated an increase in the light extraction by Bragg-scattering of waveguided light using a corrugated photoresist layer. However, in this device structure the light must transmit through the absorptive gold and photoresist layers, which limit its absolute efficiency [24]. Later, Ziebarth *et al.* [23] have demonstrated a more conventional ITO-based electroluminescent (EL) device using a stamped Bragg grating into poly(3,4-ethylenedioxythiophene)-poly(styrenesulfonate) (PEDOT:PSS) layer. Even though the soft-lithography is beneficial in fabricating large-scale devices at low cost, waveguide absorption is strong in ITO and patterned PEDOT layers [24]. This results in reduction of grating effect particularly in the shorter wavelength region. Fujita *et al*. have also shown the improved electroluminescence from a corrugated ITO device using this concept [27,28]. They have used vacuum evaporated EL materials and square-shaped pattern substrates. Using vacuum evaporation, the organic materials deposited on patterned substrates retain their pattern shape due to the low adatom mobility of deposited organic molecules. This corrugated shape through all device structure enhances the light extraction efficiency by not only waveguided light diffraction but also surface plasmon. However, a square type pattern is not suitable for fabricating stable EL devices because of possible electrical short problems.

The enhanced light extraction from OLEDs with diffractive resonators can be explained as follows. First, waveguided light propagation along the in-plane direction of the device is emitted to the surface direction by Bragg diffraction in the grating device. Figure 5 illustrates the mechanism of how the diffracted light can be extracted by Bragg diffraction in a 1-D grating sample for simple consideration. If the light incident on a material with a refractive index of n_2 from that with n_1, the diffraction condition is given by

$$m\lambda = d_c\left(n_1 \sin\theta_1 - n_2 \sin\theta_2\right)\left(\theta_1 > 0, \theta_2 < 0\right) \tag{3}$$

where λ is the wavelength, n_i (i=1 and 2) is the effective refractive index, d_c is the grating period, and m is the diffraction order. If we consider a waveguided light to have a high incident angle (θ_1~90°) and diffracted light has the lowest diffraction angle (θ_2~0°), then eq. (3) can be simplified as:

$$m\lambda = n_{eff} d_c \tag{4}$$

where n_{eff} is the effective refractive index. For m=1, first-order diffracted light can be extracted to surface normal direction resulting in an increased light extraction.

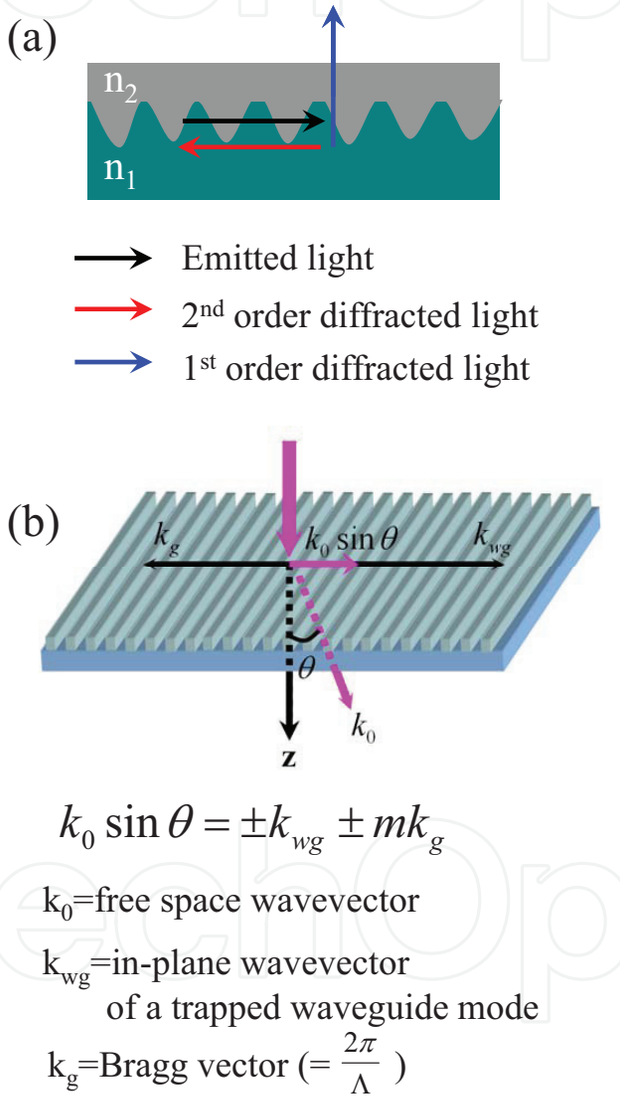

Figure 5. Typical structure of a diffractive resonator along one axis in the plane of the waveguide.[33] Copyright 2008, American Institute of Physics.

This diffraction relation can also be applied to the surface-emitting distributed feedback laser. Here we consider a situation where the waveguided and diffracted lights have high incident angles, i.e., θ_1 = 90° and θ_2 = - 90°. By substituting these angles into eq. (3), one obtains:

$$m\lambda = 2n_{eff}d_c \tag{5}$$

For m=2, second-order diffracted light makes the counter propagating mode, which results in an optical feedback for lasing. Lasing does not occur along the guided direction because of the low quality of side surfaces but it is outcoupled to the surface normal direction by first-order Bragg diffraction.

Hence, the physical meaning of this relation is that both first- and second-order Bragg diffractions of waveguided light occur simultaneously in different directions. That means waveguided light satisfying the Bragg condition is perfectly extracted toward the surface normal direction by the first-order Bragg diffraction until the second-order Bragg diffracted light decays along in-plane direction.

2.2. Device fabrication with nano-patterned structures

Nano-patterned structures are prepared to fabricate corrugated OLEDs. For periodic and quasi-periodic nano-patterned substrates, 1-D and 2-D grating and buckling structures, respectively, are prepared as described below:

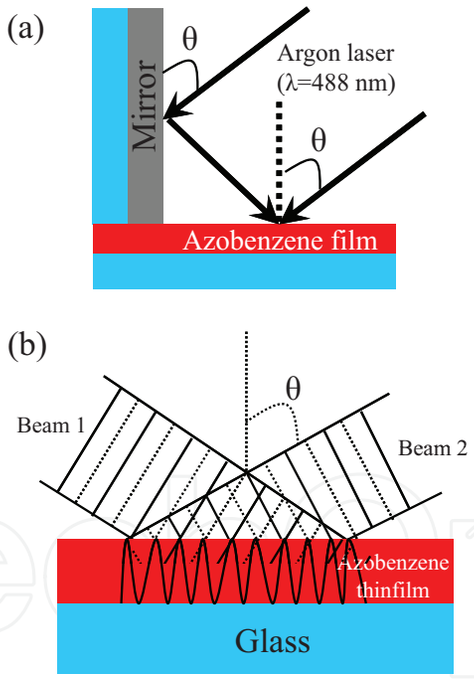

Figure 6. Schematic illustration of surface relief grating fabrication process.

To form a 1-D surface relief grating (SRG) structure, an azobenzene polymer thin film is irradiated using two Ar^+ laser (488 nm) beams. This is achieved due to the mass transport from the region of constructive interference to that of destructive interference region in azobenzene polymer, leading to a volume decrease in the highly irradiated (constructive intereference) region with the increase in the irradiation time as shown in Fig. 6. This process is quite different from the other more conventional microscopic processes such as laser ablation and chemical etching. The major advantage of this photo-fabrication approach

is the possible precise control of grating depth by adjusting the light exposure energy and polarization states of writing beam.

The two recording lights are circularly polarized. Based on the following equation, the periodicity of the SRG can be controlled by changing the crossing angle between two recording laser beams.

$$\Lambda = \frac{\lambda_{laser}}{2\sin\theta} \tag{6}$$

where λ_{laser} is the wavelength of the laser and θ is an incidence angle. The formed SRG pattern is transferred onto a UV curable epoxy or a CYTOP (perfluoropolymer, Asahi Glass Co. Ltd.,), so that a patterned substrate with an SRG is obtained.

For a buckling fabrication, standard commercial poly(dimethylsiloxane) (PDMS) materials (Wacker ELASTOSIL RT 601) are mixed with a curing agent in a weight ratio of 9:1 and then spin-coated on a pre-cleaned glass substrate. The coated PDMS is cured at 100 °C for 1 h and then an aluminum layer is deposited on it. A structure thus prepared is heated to 100 °C with an external radiation source by thermal evaporation at a pressure below 1×10^{-3} Pa. It is then cooled to the ambient temperature by keeping it in a chamber for more than 30 min and venting to atmosphere. The difference in the thermal expansion coefficients between the aluminum film and PDMS generates a buckled structure on the PDMS film. The PDMS replica is formed by pouring PDMS over the buckled PDMS master and by curing it at 100 °C for 1 h. The PDMS replica can be easily peeled off from the PDMS master. For the second deposition of a 10-nm-thick aluminum layer, the buckled PDMS replica is used as the substrate. After deposition, the buckling pattern of the replica is transferred to a glass substrate after UV curing in curable resin (Norland Optical Adhesive 81) for 10 min. For the third deposition of a 10-nm-thick aluminum layer, the buckled PDMS replica thus fabricated is used as the substrate, and the above process is repeated. After the deposition, the buckled resin master is again produced, from which, finally, the buckled PDMS replica mould for making devices is fabricated.

The method of replicating nano-patterned structures (azobenzene film and buckling) onto substrates is shown in Fig. 7 [34]. First, the patterned azobenzene polymer film or buckling pattern is converted to a master mould of PDMS. After the heat treatment at 50 °C for 1 h the silicon rubber becomes firm and it can easily be separated from azobenzene polymer substrate as a free-standing film. The CYTOP solution (CTL-109A, Asahi Glass Co. Ltd.) is drop-cast on a glass substrate and is heated under the patterned silicon rubber mould pressed on it at 60 °C for 1 h. For the UV curable epoxy (Norland Optical Adhesive 81), UV light is irradiated to harden the epoxy layer under silicon rubber mould. The patterned structure is thus replicated onto a substrate.

We fabricated OLEDs on patterned nano-structured substrates. The device structures introduced in this chapter are classified in two parts, organic and polymeric devices. The organic layers in the organic device are coated by thermal evaporation (2-D grating & buckling devices), whereas spin coating (1-D grating device) is used in the polymeric device.

However, the basic concept is almost the same in both cases except for deposition method and materials used.

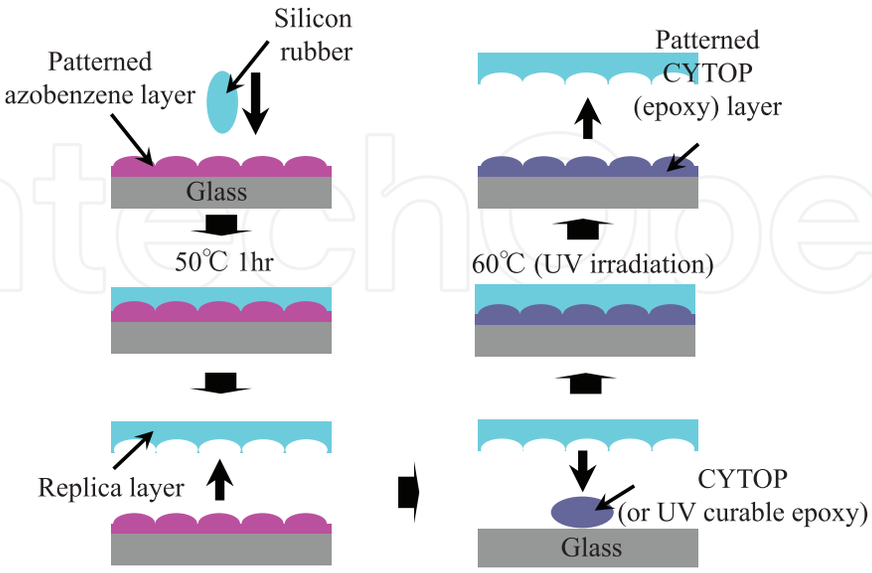

Figure 7. Schematic diagram of nano-imprint process.[34] Copyright 2008, American Institute of Physics.

We prepared ITO or Au stripes as an anode using sputter deposition or thermal evaporation. In case of organic EL devices, a two or three-layered structure consisting of (CuPc: used in 2-D grating device))/TPD/Alq3 is deposited successively by vacuum evaporation. For making the polymeric EL device, PEDOT doped with poly-(styrenesulfonate) PSS is spin coated as a hole transport layer (HTL) and heated at 60 °C for 20 min (T_g of CYTOP : 108 °C) in an oven. Then MEH-CN-PPV is spin coated as an emissive layer (EML) on the HTL successively.

After coating organic or polymeric layers using a metal mask, lithium fluoride (LiF) as an electron injection layer (EIL) and Al as a cathode are deposited. The detailed experimental conditions including thickness of each layer were explained elsewhere [33,35,36]. The pixel with a size of 3 mm×3 mm was used for electroluminescence measurements.

2.3. Effects of periodic DFB grating structures in OLEDs

In this section, we examine light extraction characteristics from OLED devices with 1-D or 2-D DFB grating substrates. The waveguided light is extracted to normal direction by an imprinted low-refractive index layer (1-D DFB grating). Also, electrical characteristics in OLEDs with 2-D hexagonally nano-imprinted periodic structures are investigated to confirm the enhanced light extraction from this device (2-D DFB grating). We review previously reported results in view of light extraction characteristics and electrical characteristics from periodically corrugated OLEDs.

Optical characterization of corrugated OLEDs with periodic structures (1-D grating): Figure 8(a) shows a schematic illustration of the Bragg diffraction process of waveguided light in periodic structures. When waveguided light is incident on the grating structure, the light is reflected by

a photonic band gap and simultaneously diffracted in the direction perpendicular to the photonic crystal surface because the Bragg condition is satisfied in this direction. The angle θ of the emission direction with respect to the surface normal is governed by the conservation of momentum in the plane of the waveguide [21-24,37,38] given by

$$k_0 \sin\theta = \pm k_{wg} \pm k_g = \pm \frac{2\pi n_{eff}}{\lambda} \pm m\frac{2\pi}{\Lambda} \quad (7)$$

where λ is the wavelength, k_{wg} and k_g are respectively the wavenumbers of the waveguided light and the grating with a period Λ, n_{eff} is the effective refractive index of the waveguide mode, k_0 is the free-space wavenumber of the diffracted light, and m is the diffraction order. If Λ and n_{eff} are known, eq. (7) gives the emission angle of extracted light as a function of wavelength for the first-order Bragg diffraction of waveguided light.

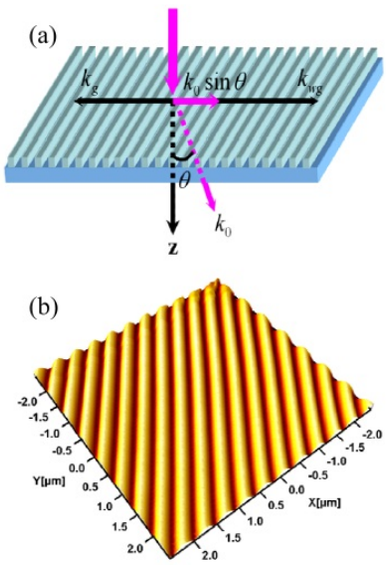

Figure 8. (a) Schematic illustration of Bragg diffraction of waveguided light. (b) AFM image of patterned azobenzene polymer.[33] Copyright 2008, American Institute of Physics.

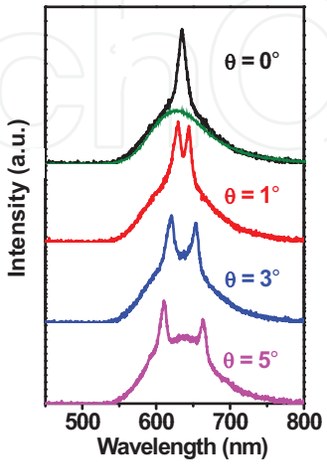

Figure 9. Angular dependence of electroluminescence spectra from OLED devices with flat (green curve at θ =0°) and patterned CYTOP layer.[33] Copyright 2008, American Institute of Physics.

Figure 9 shows the angle dependence of EL spectra for the two EL devices with and without the grating structure. For measuring the EL spectra, a detector with a diameter of 5 mm is located 10 cm apart from the device surface. A sharp peak (632 nm) has been observed in the normal direction (θ =0°), and a peak splitting has been found to occur by increasing the detection angle because the grating diffracted waveguided light travels in the opposite direction. The wavelengths of the separated two peaks have been measured as a function of the detection angle as shown in Fig. 10(a). The measured wavelength positions agree well with the lines given by eq. (8) with θ_3, which is given by

$$\theta_3 = \arcsin\left(\frac{n_2}{n_3}\sin\theta_2\right) = \arcsin\left(\frac{n_2}{n_3}\sin\left(\arcsin\left(\frac{n_1}{n_2}\sin\theta_1\right)\right)\right) \quad (8)$$

considering all refractions in PPFVB/glass/air, as shown in Fig. 10(b). This means that extraction angle of Bragg diffracted light is closely related to refractive indices of stacked materials.

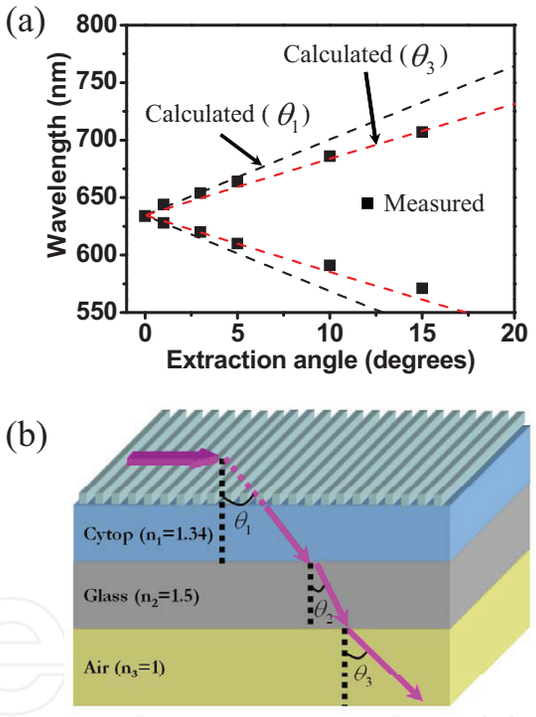

Figure 10. (a) Measured extraction angles of Bragg diffracted light. θ_1 and θ_3 denote calculated extraction angles in CYTOP and air, respectively. (b) Schematic illustration for refraction of Bragg diffracted light in each stacked material.[33] Copyright 2008, American Institute of Physics.

To compare the effects of refractive indices of imprinted materials, we have calculated light extraction angles from materials with various refractive indices, as shown in Fig. 11. The wavelength of vertically emitted light is assumed to be 632 nm. According to eq. (8), as the refractive index becomes high, the light extraction angle becomes wider. For n=1.80, the extraction angle of light with wavelength of 800 nm is 65°, whereas the total light extraction angle is only 23° for n=1.00. In the case of CYTOP (n=1.34), the total light extraction angle is

35°. Thus nano-imprinted CYTOP layer can extract waveguided light with high directionality. Such characteristics provide an advantage for small- or medium-size OLEDs, which are mainly viewed from the forward direction [39].

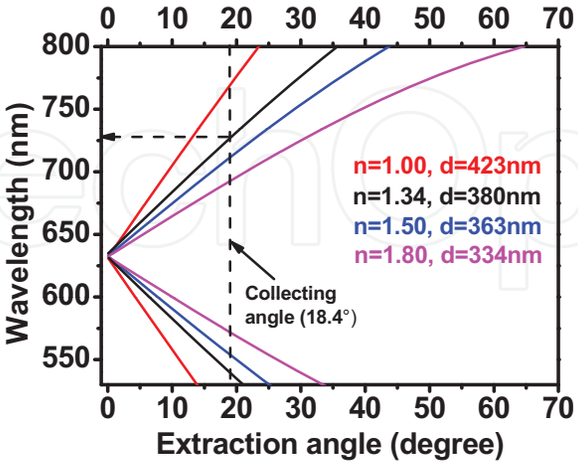

Figure 11. Calculated extraction angles in imprinted materials with various refractive indices as a function of wavelength.[33] Copyright 2008, American Institute of Physics.

The effect of a grating on normally-directed EL has been observed by collecting EL spectra between ±18.4°, as shown in Fig. 12. The enhancement of EL spectra in the device with patterned CYTOP layer has been observed over the wavelength range from 540 nm to 728 nm. However, it should be noted that the highest EL intensity is observed only around 650 nm, whereas vertically directed emission peak position is 632 nm. This results from different transmittance of ITO at various wavelengths as shown in Fig. 12. Because the wavelength of the highest EL intensity is closely related to both natural fluorescence and waveguide absorption in ITO layer, the light can be extracted more efficiently due to the high transmittance and fluorescence at 650 nm. Hence, the grating effect is higher in longer wavelength region which has higher transmittance. If ITO with high transparency is possible to be deposited at room temperature, the grating effect of CYTOP with high transmittance will be increased.

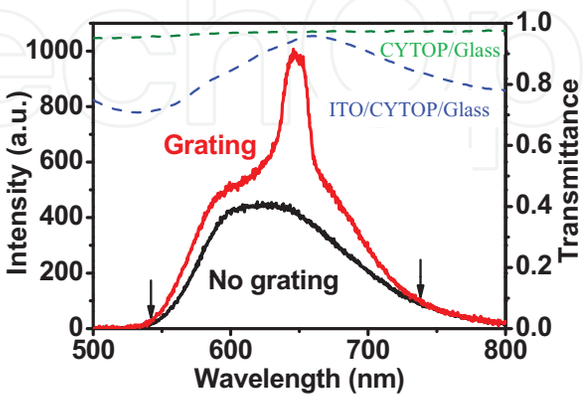

Figure 12. Overall EL spectra within ±18.4° from OLEDs with flat and patterned CYTOP layers. Two dotted lines show transmittance of CYTOP/Glass and ITO/CYTOP/Glass, respectively.[33] Copyright 2008, American Institute of Physics.

Electrical characterization of corrugated OLEDs with periodic structures (2-D grating): The current–voltage (I-V) characteristics of an EL device with a 2-D grating (2-D grating device) has been measured and compared with those of an EL device without grating (non-grating device). The 2-D grating device shows a higher current level compared to the non-grating device, as shown in Fig. 13(a). Both EL devices show a power-law dependence of $I \sim V^{6\text{-}7}$ over a large current and voltage range. Because of large trap concentration and low mobility in organic semiconductors, the carrier transport in OLEDs is trap-charge-limited current (TCLC) [40], which is known to show power law dependence.

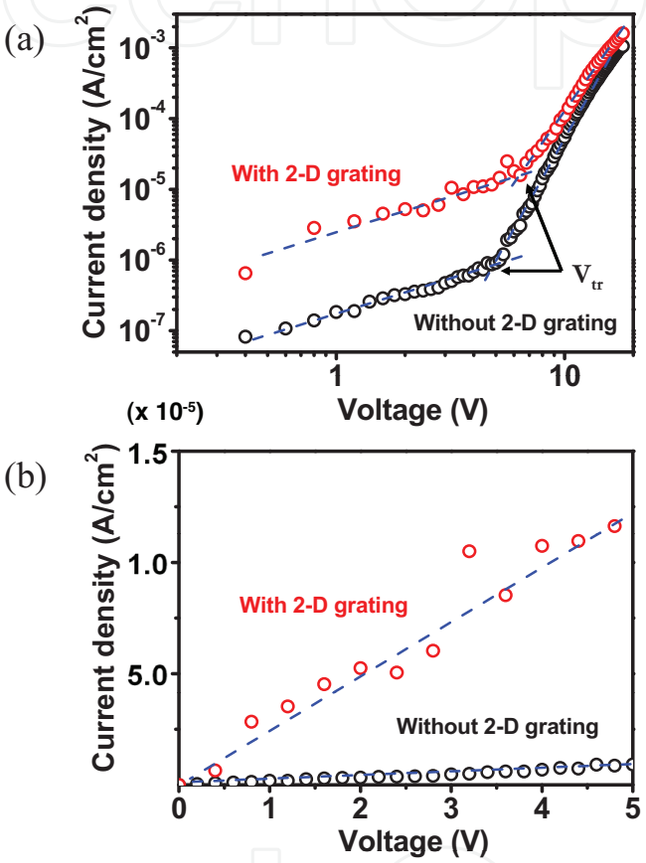

Figure 13. (a) Current-voltage plot measured from a 2-D grating and non-grating devices. (b) Magnified current-voltage plots in low voltage region.[35] Copyright 2008, The Japan Society of Applied Physics.

One may intuitively think that higher current effect in 2-D grating devices is simply due to the increase of interface contact area by corrugation between electrode and organic semiconductors. However, this cannot explain the increase of transition voltage (V_{tr}) at which the conduction model changes from ohmic to TCLC, as indicated by two arrows in Fig. 13(a). If the increase in the interface contact area is a major effect, V_{tr} in the grating device must be shifted to a voltage lower than that of the non-grating device because higher current must satisfy TCLC conduction more quickly.

At low voltages, low-mobility ohmic conduction via thermally generated free charge is observed. In this case, the current density J is described by

$$J = q\mu_n n_0 V / d_t, \tag{9}$$

where q is the electronic charge, μ_n is electron mobility, n_0 is a thermally generated background free charge density, V is the applied voltage, and d_t is the organic layer thickness. In order to find what induces the low voltage ohmic current, we have examined the *I-V* plot in the low voltage range. According to Fig. 13(b), the 2-D grating device shows a higher ohmic current than that of the non-grating device. This means that the 2-D grating device has a lower total resistance R_{total} which is a sum of junction resistance (R_J), bulk resistance (R_B) of organic layers and electrode resistance (R_{EL}) and is given by:

$$R_{total} = R_J + R_B + R_{EL} \tag{10}$$

Here the ohmic resistance induced by Al and Au (R_{EL}) and the junction resistance (R_J) induced by interfacial barrier between electrode and organic layer are the same in both samples. Hence R_B in the 2-D grating device must be smaller than that in the non-grating device. This result may be understood from the concept of 'partial reduction thickness of organic layers' proposed by Fujita *et al*. [27,28]. They have observed improved electroluminescence from a corrugated ITO where the reduction of thickness of organic layers is effectively induced by each edge of Al and ITO square-shape patterned electrodes shown as black areas in Fig. 14(a). At the edge of each patterned electrode, a higher electric field develops (See Fig. 14 (a)) and this results in reduction of operating voltage. Thus, the increased low voltage current in the 2-D grating device may be explained due to the lower bulk resistance (R_B) and hence the lower total serial resistance.

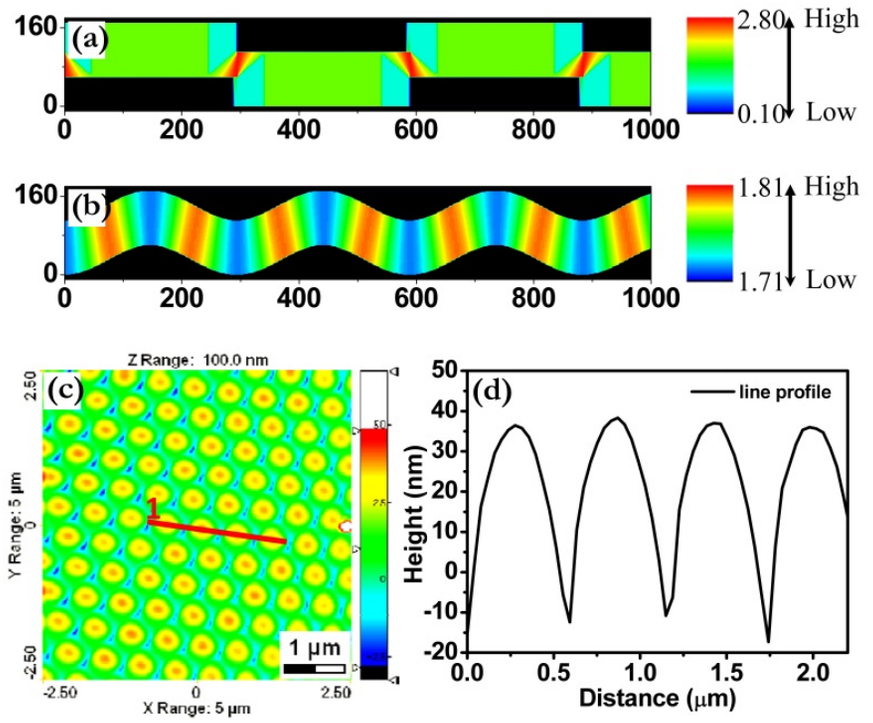

Figure 14. Calculated static field distribution between (a) square- and (b) sinusoidal-shape patterned electrodes. (c) AFM image of a patterned UV epoxy layer. (d) Depth profile along a red line in (c).[35] Copyright 2008, The Japan Society of Applied Physics.

Even though the depth of patterned shape is only 50 nm, the 2-D grating device does not show any breakdown during applying voltage. Generally thin EL devices can easily suffer from breakdowns because the internal field distribution is very sensitive to interface roughness and dust particles. It is therefore very important that the patterned electrode shape must be optimized for the stability of EL devices. Otherwise, the patterned electrode may result in worse device condition without realizing any high light extraction efficiency. Because of this reason, one should use those patterned electrode structures which give minimal 'partial reduction thickness of organic layers'. This means that if the field distribution between cathode and anode is uniform, the possibility of breakdown may be reduced even when the depth of patterned shape is high. For studying the effect of the shape of patterned electrodes, we have calculated the static field distribution in EL devices for patterned electrodes of square and sinusoidal shapes. Although the light is diffracted by 500-nm-pitched lines, which has the same width as the interfered periodicity of the two Ar^+ laser beams (Fig. 6(b)), the electric field distribution is related to the distance between closest protrusions. Hence the distance used for the calculation is 580 nm. (See Fig. 14(c)). As shown in Fig. 14(a), a high electric field gets localized at the edges of square-shaped cathode and anode electrodes. However, if the patterned electrodes are of sinusoidal shapes the field distribution becomes almost uniform. Figure 14(b) shows static field distribution in sinusoidal-shaped electrode. Note that we use different ranges of relative field intensity in Fig. 14(a) and (b) to clearly visualize the field distribution as color variations. Although the field is concentrated in the intermediate regions between the top and bottom of the patterned electrodes (see Fig. 14(b)), the field distribution becomes much more uniform compared with the case of Fig. 14(a). Figure 14(d) represents the depth profile of a patterned azobenzene film obtained along a red line in the AFM image shown in Fig. 14(c). The shape at the upper region is approximated as sinusoidal. This shape results in no breakdown of 2-D grating devices even though leakage current is high.

Next, we describe the relationship among the reduction of thicknesses, current efficiency, and diffraction effects. Figure 15(a) displays the external current efficiency versus current density. In the 2-D grating device, a higher efficiency is obtained in a high current density region. However, below a current density of 3×10^{-5}A/cm^2, the efficiency of the non-grating device is found to be slightly higher than that of the 2-D grating device, as shown in Fig. 15(b). How can we explain this? As mentioned above, the major difference between a 2-D grating device and a non-grating device is in R_B or effective thickness of the bulk layer; i.e., R_B is lower and the layer is thinner in the 2-D grating device than that in the non-grating device. Hence, we should discuss the dependence of current efficiency on the emitter thickness [41]. For this purpose, the recombination probability (P_{rec}), which is directly proportional to the EL yield, is considered. P_{rec} is defined by the ratio of the recombination time τ_{rec} and the transit time τ_t of the charge carriers as:

$$P_{rec} = \tau_t / \left(\tau_t + \tau_{rec}\right) = 1 / \left(1 + \tau_{rec} / \tau_t\right) \tag{11}$$

This gives $P_{rec} = 1$ when $\tau_{rec}/\tau_t=0$ and P_{rec} decreases with increasing τ_{rec}/τ_t. The thickness dependence in τ_t comes only from:

$$\tau_t = d_t / \mu F, \tag{12}$$

where d_t is the emitter layer thickness, μ the carrier mobility, and F the applied electric field operating on the sample. According to eqs. (11) and (12), at a given electric field, increasing emitting layer thickness will increase τ_t and hence P_{rec}. Employing this theory, 2-D grating device must show lower current efficiency due to the short transit time by reduction of thickness.

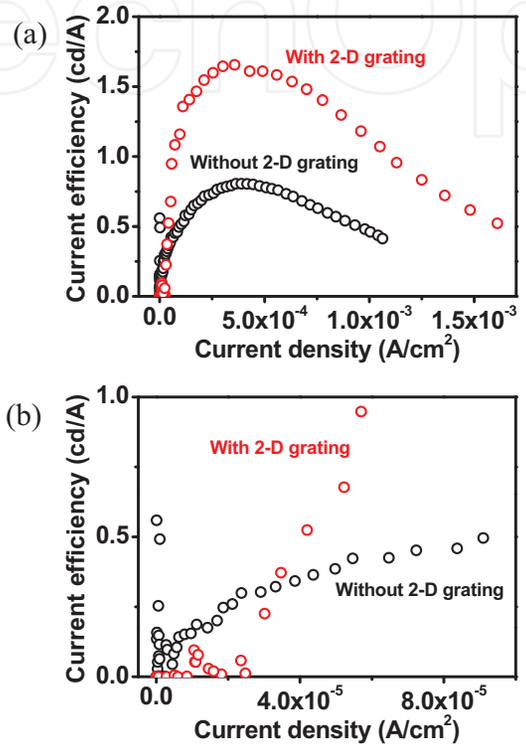

Figure 15. (a) Extracted current efficiency against current density measured from a 2-D grating and non-grating devices. (b) Magnified extracted efficiency vs current density in low current density region. [35] Copyright 2008, The Japan Society of Applied Physics.

It should be noted, however, that a higher current efficiency in the 2-D grating device increases even though the non recombined current is higher. The enhanced current efficiency in the 2-D grating device can be explained as follows. First, the waveguided light propagating along the in-plane direction of the device is emitted to the surface direction by Bragg diffraction in the 2-D grating device. Figure 16(a) shows how the diffracted light can be extracted by Bragg diffraction in a 1-D grating sample for simple consideration. If the light incident on a material with the refractive index of n_2 from that of n_1, the diffraction condition is given by

$$m\lambda = d_c(n_1 \sin\theta_1 - n_2 \sin\theta_2) \tag{13}$$

where d_c is a periodic distance and m is a diffraction order. Because the refractive indices are n_1=1.7 and n_2=1.5 in EL layer and epoxy/glass, respectively, the 1st-order diffracted light (m = 1) can be emitted, as shown in Fig. 16(b) and (c). In flat devices without grating, only EL

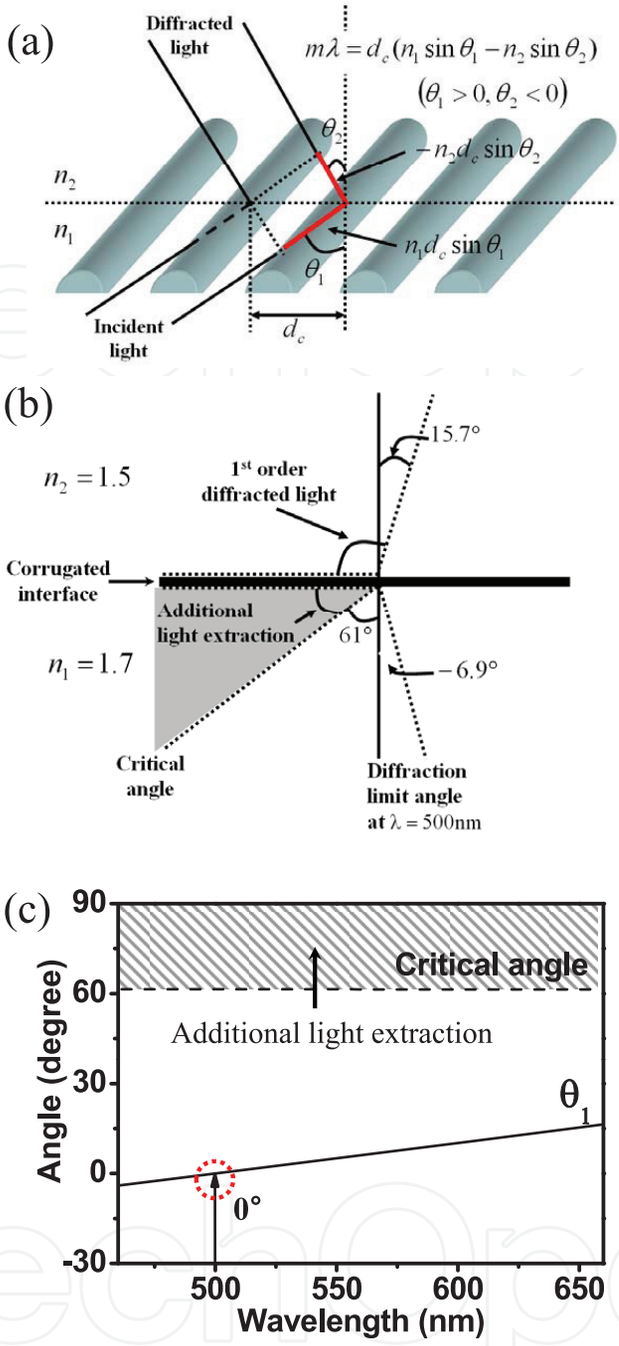

Figure 16. (a) Schematic illustration of diffraction of the guided light. (b) Schematic illustration of the angle range for total reflection and diffraction at 500 nm wavelength. (c) The diffraction limit of incidence angle θ_1 for the first diffraction as a function of wavelength. [35] Copyright 2008, The Japan Society of Applied Physics.

light to an angle below the critical angle (61°) can be emitted due to the total internal reflection. However, in grating devices, the incident light within the angle range between θ_1 and 90° is diffracted and then emitted at an angle between θ_2 and -90°. For example, in the case of a light with 500 nm wavelength, θ_1 and θ_2 are 0° and 7.6°, respectively. This means that the incident light within the angle range between 0° and 90° can be emitted at an angle

in the range between 7.6° and -90°. It should be noted that an incident light within 61°~90° cannot be emitted in flat devices without a grating. In other words, the light diffracted from the incidence angle in the range between 61° and 90° contributes to additional light extraction in 2-D grating devices obtained, resulting in an increase in the of light output.

Another aspect of enhancing the light extraction in a 2-D grating device is by recovering the quenched light coupled with surface plasmon mode. This effect can be observed in an Alq_3-based system because the excitons have no preferred orientation in an Alq_3 layer, whereas conjugated polymer systems show a lower effect because the dipole moments lie in the plane of the film due to spin casting. Hobson *et al*. [42] have found that a further recovery of the trapped light can be obtained by the surface plasmon with the help of a periodic grating formed on substrate particularly in Alq_3-based EL devices. This effect can also explain the increased current efficiency in Alq_3-based EL devices because the corrugation remains intact on the Al electrode layer.

2.4. Effects of quasi-periodic buckling structure in OLEDs

Buckling patterns are produced spontaneously by thermal evaporation of Al films on poly(dimethylsiloxane) (PDMS) substrates preheated to 100 °C using an external heat source. Al layers with a thickness of 10 nm are deposited on thermally expanded PDMS. After cooling to ambient temperature, the buckling process spontaneously occurs, releasing the compressive stress induced by the difference between the thermal expansion coefficients of PDMS and Al films [43-45]. Figure 17(a), (b) and (c) shows atomic force microscopy (AFM) images of buckles formed by a 10-nm-thick Al layer applied once, twice and three times, respectively. The vague symmetric ring in the fast Fourier transform (FFT) pattern shows that the buckling structure has a characteristic wavelength with a wide distribution and without preferred orientation of the periodic structure. The characteristic wavelength can be obtained by the power spectrum of FFT as a function of wavenumber $k=2\pi/\lambda$. Figure 17(d) presents the power spectra of various buckles plotted against the wavelength instead of the wavenumber for direct comparison with outcoupled spectra of OLEDs. The buckling structure of the 10-nm-thick Al layer shows a peak periodicity at wavelengths of ~400 nm (Fig. 17d), resulting in a ~1.4% increase in the surface area ratio of the buckled to flat PDMS with a buckle depth as low as 25–30 nm as shown in Fig. 17(a).

In general, the depth of buckling structure D depends on the buckling periodicity λ, which is proportional to the thickness d of thin films and the imposed compressive strain (stress) Δ as $D \sim \lambda\ \Delta^{1/2}$ [46,47]. The buckles need to have a large depth for efficient diffraction and require a shorter buckling periodicity than that shown in Fig. 17(a) to be effective for an emission peak at a wavelength of ~525 nm. However, there is a trade-off between these factors, because D is proportional to λ. We have therefore adopted an alternative method assuming that the larger the compressive stress, the deeper are the buckles at a constant wavelength [48]. We have introduced additional compressive stresses by further deposition of a 10-nm-thick Al layer, once or twice more, on a buckled PDMS replica fabricated from a buckled PDMS mould after the first deposition of an Al layer (Figs. 17(b) and (c)).

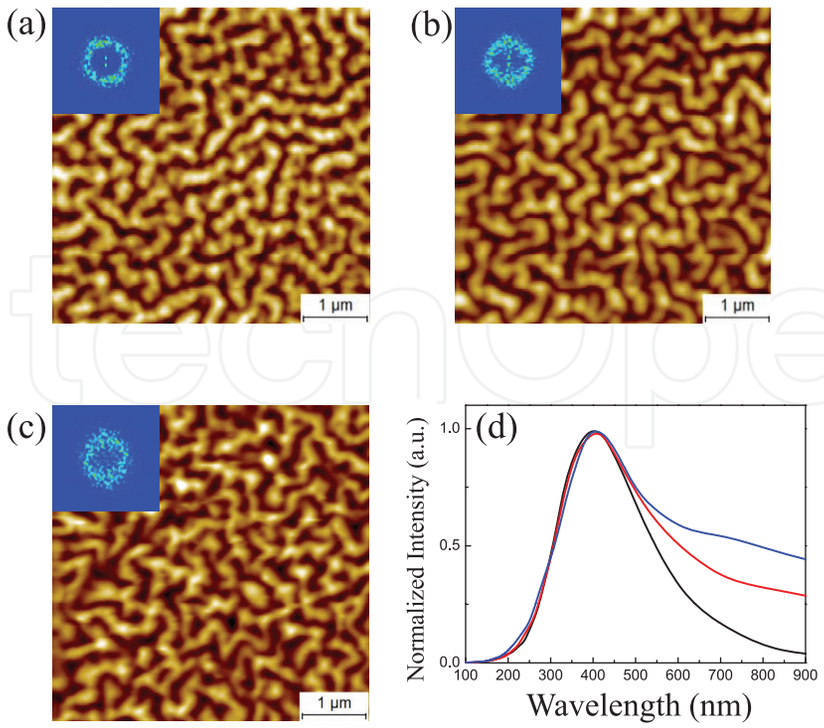

Figure 17. AFM analysis of buckling pattern. (a) Buckled structure formed by a 10-nm-thick Al layer. (b),(c) Buckled structures formed by deposition of a 10-nm-thick Al layer twice and three times, respectively. Resin layers imprinted with a buckled PDMS replica were used for measurement. Inset: FFT patterns of each image. (d) Power spectra from FFTs as a function of wavelength for buckled patterns obtained with deposition of a 10-nm-thick Al layer once (black), twice (red) and three times (blue).[36] Copyright 2010, Nature Publishing Group.

The observation that the FFT ring patterns are of similar size indicates that the characteristic wavelength does not change after redeposition. Moreover, the FFT ring patterns after multiple deposition processes display more diffuse patterns, indicating a broader distribution. The power spectra in Fig. 17(d) represent the unchanged peak wavelengths at ~410 nm and the broader distributions in the long wavelength side for the multiple depositions. In addition, the surface area ratio after deposition twice and three times significantly increases from ~1.4% to ~9.0% and 11.3% corresponding to depths of 40–70 nm and 50–70 nm, respectively.

The devices with buckling show higher current density (*J*) and luminance (*L*) than those without buckling and a device with triple buckling shows higher *J* and *L* than that with only double buckling (Fig. 18(a)). It has been reported that the larger *J* in the corrugated device mainly results from a stronger electric field because of the partially reduced organic layer thickness in the intermediate region between the peak and valley of the sinusoidal patterned gratings [27,35]. Measurements have also been made on devices without buckling but with the organic layer thickness decreased by 20% and 40%. As mentioned in 2.3, current density (*J*) for these devices is shown by dotted and dashed curves in Fig. 18. The current density in the device with triple buckling lies between that in the reference devices and in devices with thinner organic layers. This suggests that the thickness of the organic layers on buckling is partially reduced by ~20–40%. In the devices with double, triple and without buckling, the

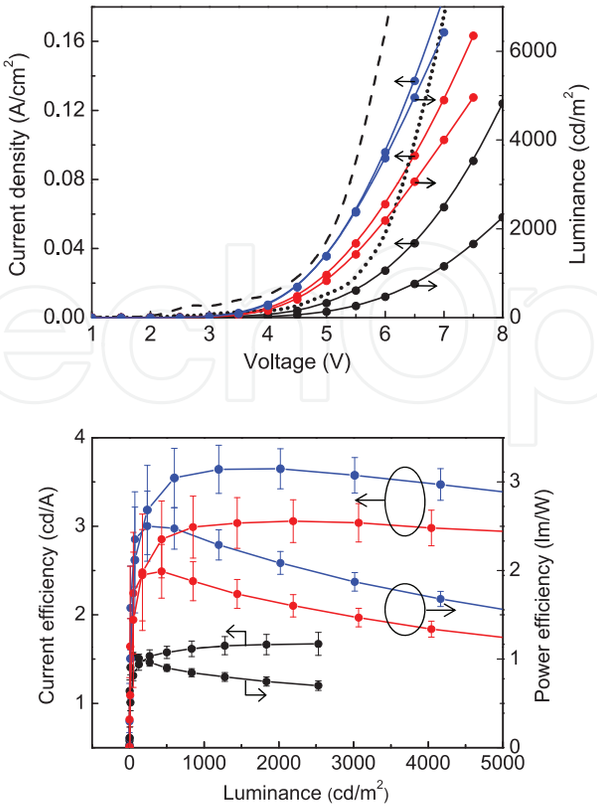

Figure 18. Device performance. (a) Current density–luminance–voltage characteristics of typical OLEDs without buckling (black) and with double (red) and triple (blue) buckling. The dotted and dashed lines represent the current density of devices without buckling but with the organic layer thickness decreased by 20% and 40%, respectively. (b) Current efficiency (cd/A) and power efficiency (lm/W) as a function of luminance (cd/m²) for OLEDs without buckling (black) and with double (red) and triple (blue) buckling. [36] Copyright 2010, Nature Publishing Group.

current efficiencies are found to be 3.05 cd/A (double buckling), 3.65 cd/A (triple buckling) and 1.67 cd/A (without buckling), and the power efficiencies 1.64, 2.1 and 0.73 lm/W, respectively, at a luminance of 2,000 cd/m². These efficiency increases correspond to enhancements of ~83% with double buckling, and 120% with triple buckling in the current efficiency and 120% with the double buckling and 190% with triple buckling in the power efficiency (Fig. 18(b)). We attribute the greater enhancement of efficiencies in the devices with triple buckling than those in double buckling to an increase in the optical confinement factor due to the greater buckling depth [28]. The observed enhancement in the power efficiency higher than in the current efficiency may be attributed to the reduction in operating voltage due to the partial decrease in the organic layer thickness in the corrugated structure (see Fig. 18(a)). One may expect that the decreased thickness of the N,N'-bis(3-methylphenyl)-N,N'-diphenylbenzidine (TPD) and Alq_3 layers may lead to a better charge balance with a better internal quantum efficiency because of the stronger electric field dependence of electron mobility in the Alq_3 layer than that of hole mobility in the TPD layer. However, the devices without buckling but with decreased thickness of the organic layer show no improvement in the current efficiency. The device with a decrease in thickness of 40% shows a significantly decreased current efficiency of 0.86 cd/A at 2,000 cd/m². This is

consistent with the reported studies in which, as the Alq_3 layer thickness decreases below 30 nm, the carrier recombination probability decreases and the exciton-quenching effects at the Al cathode increase, thereby decreasing the internal quantum efficiency of the devices [25,40,49,50]. Therefore, the great enhancement of current and power efficiency in the devices with buckling is obviously caused not by a change of internal quantum efficiency, but by an increase in the outcoupling efficiency, that is, enhanced extraction of the waveguide light.

To investigate the outcoupling of the TE_0 and TM_0 modes, we have measured the electroluminescence spectra of these devices. Contrary to the enhancement emerging as new sharp peaks in conventional corrugated OLEDs [21-24,27,28,33], our buckled devices exhibit enhancement over the entire electroluminescence spectrum (Fig. 19(a)). We have evaluated

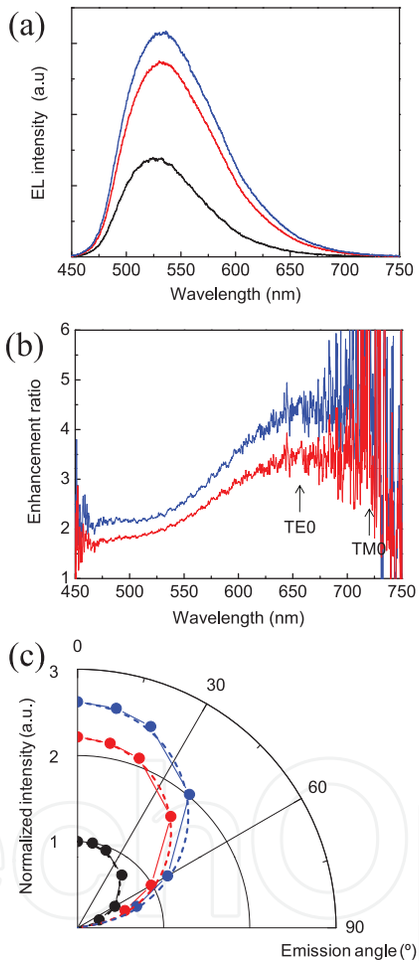

Figure 19. Electroluminescence spectral characteristics. (a) Electroluminescence spectra of devices without buckling (black) and double (red) and triple (blue) buckling, measured from the surface normal at a current density of 5 mA/cm². (b) Enhancement ratio of intensity by buckling as a function of emission wavelength, obtained by dividing the spectrum of the device with double (red) and triple (blue) buckling by that without buckling. The wavelengths of the TE_0 and TM_0 modes are indicated by arrows at 655 and 720 nm, respectively. (c) Angular dependence of light intensity for devices without buckling (black) and with double (red) and triple (blue) buckling. All data were normalized with the intensity of the devices without buckling in the normal direction. Each dashed line represents a guide to the ideal Lambertian emission pattern. All devices with and without buckling show the Lambertian emission pattern with a maximum intensity in the normal direction.[36] Copyright 2010, Nature Publishing Group.

the wavelength dependence of the enhanced emission by considering the intensity ratio of the two spectra in the devices with and without buckling (Fig. 19(b)). The calculated peak wavelengths of the TE_0 and TM_0 modes for the first-order diffraction are consistent with the broad peak intensities in Fig. 19(b), although the enhancement due to the TM_0 mode is not distinct because of the weak emission intensity above 700 nm. The relatively flat enhancement by a factor of ~2.2 around λ_0=525 nm in the devices with triple buckling is partially due to the relatively weak first- and second-order diffraction TE_0 and TM_0 modes, whereas the remarkable enhancement (factor of 4.0) around 655 nm is mainly due to the strong first-order diffraction in TE_0 and TM_0 modes (see Fig. 19(b)). These results indicate that a further enhancement of more than a factor of at least 2.2 can be expected if the peak wavelength of the buckles is optimized for the TE_0 and TM_0 modes to be diffracted at around 525 nm in the normal direction. Moreover, the broad distribution of periodicity in the buckling structure suggests that the entire emission wavelength range over blue, green and red in white OLEDs can be simultaneously outcoupled by only one grating structure. The angular dependence of the light intensity for the devices is shown in Fig. 19(c). It is interesting to note that all devices with and without buckling show a Lambertian emission pattern with a maximum intensity in the normal direction. According to the Bragg equation, the first-order diffraction angles of the TE_0 and TM_0 modes around the main emission wavelength of 525 nm by the grating period of 410 nm are expected to be between 20° and 40°. However, because k_G has random orientation and broad periodicity due to the buckling, it is distributed over all azimuthal directions in contrast to one- or two-directional k_G in conventional corrugated OLEDs [21-24,27,28,33]. Thus, the outcoupled emission concentrates into the normal direction, resulting in the Lambertian emission pattern.

3. Polarized electroluminescence

The polarization control of light is important for optical information processing, display and storage devices. Although linearly polarized light has already been applied to various optical devices, there are only a few reports on circularly polarized devices. However, the potential applications of circularly polarized light have been suggested for optical data storages and flat panel displays. Recently, the research for active devices that can emit polarized light has gained attention [51-58]. Peeter *et al.* [56] have first demonstrated circularly polarized (CP) EL from a polymer LED using a chiral π-conjugated poly(*p*-phenylenevinylene) (PPV) derivative as an active layer, although the degree of circular polarization was very low. Later, Oda *et al*. [57] have succeeded in obtaining a high CP-EL using main-chain polymer liquid crystals (LCs) and chiral-substituted polyfluorenes (PF) as an active layer. However, the degree of circular polarization was still insufficient for applications in optical devices. More recently, Grell *et al.* [58] have proposed a new idea for CP-EL without using chiral active materials and succeeded in achieving high degree of circular polarization. They used a simple CP-EL device that can be driven by nonchiral polymer LED using "photon recycling" concept developed by Belayev *et al.* [59]. Belayev *et al*. and Grell *et al*. used a chiral nematic liquid crystal (cholesteric liquid crystal; CLC) cell attached to the glass side of polymer LED and obtained a high degree of circular polarization at the center of the stop band. However, the degree of circular polarization

outside of the stop band rapidly decreased, because the emissive material had wider emission band than the stop band width formed.

For evaluating the degree of circular polarization at a certain wavelength λ, a g-factor is used which is defined as:

$$g(\lambda) = 2\frac{I_L(\lambda) - I_R(\lambda)}{I_L(\lambda) + I_R(\lambda)} = 2\frac{r(\lambda) - 1}{r(\lambda) + 1} \tag{14}$$

where $I_{L/R}$ is the intensity of left/right-handed CP (L-CP, R-CP) light, and r is the left/right-handed intensity ratio, $I_L(\lambda)/I_R(\lambda)$. It is evident that $|g(\lambda)|$ is zero for nonpolarized light ($r(\lambda)=1$) and is equal to -2 for pure, single-handed circularly polarized light ($r(\lambda)= \infty$ or 0). The $g(\lambda)$ values found were 0.001 [56], 0.25 [57], and 1.6 [58], but only in a narrow wavelength range. Woon *et al.* and Geng *et al.* respectively reported circularly polarized PL [60] and EL [61] with a constant $g(\lambda)$ value over a wide spectral range covering most of the emission band. However, the bandwidth [60] and $g(\lambda)$ value [61] were still insufficient for application to commonly used emissive materials with wide emission band.

To achieve a tunable polarization of electroluminescence, we have used combination of voltage dependent nematic liquid crystal (NLC) phase retarders and photon recycling concept [62,63]. The phase retardation arises between two optical eigenmodes during light propagation in an anisotropic medium as a phase retarder. Upon emerging from the phase retarder, the relative phase of the two eigenmodes is found to be different from that at the incidence, and thus their polarization state becomes different as well [64-66]. Now suppose we apply a voltage (V) across the cell filled with NLC, by which the liquid crystal molecules change their orientation toward the field direction, if the NLC has positive dielectric anisotropy. With increasing the voltage, the birefringence $\Delta n(E) = n_e(E) - n_0$ decreases, where n_e and n_o are refractive indices for extraordinary-(e-) and ordinary-(o-) light waves, respectively, and the retardation ($\Delta\varphi$) decreases as well. Hence, as the e- and o-waves propagate through the NLC cell, their relative phase difference changes, and the state of polarization of the wave also changes.

We have introduced another polarization characteristics, namely polarization conversion in surface plasmon (SP) coupled emission by buckling structures. In section 2.4, we have demonstrated that the quasi-periodic buckling structures with broad distribution and directional randomness can effectively enhance the light-extraction efficiency by outcoupling the waveguide modes without introducing spectral changes and directionality [36]. In this study, however, we could not differentiate the outcoupling of transverse electric (TE) mode from that of the surface-plasmon (SP) mode (transverse magnetic (TM) mode) by buckles because of the broad periodicity of the buckling structure and the similar propagation vectors of the TE and SP modes. The explanation of polarization conversion in the surface-plasmon-coupled emission presented here is based on a trial method for distinguishing TE and TM modes in light enhancement in OLEDs with buckling pattern. However in this trial approach, an interesting phenomenon of polarization conversion in SP coupling has been observed.

In this section, we have summarized and introduced our studies regarding not only circularly polarized EL and its tunability but also the polarization conversion in surface coupled emission from corrugated OLEDs with buckling structures.

3.1. Device fabrication

We have fabricated multi-layered polymer CLC (PCLC) films for using them as wide-band reflectors or single-layered films for polarization-tunable OLEDs. As an experimental method for fabricating single-layered PCLC films is a part of fabricating multi-layered PCLC films, we introduce here only the fabrication of multi-layered films and skip the fabrication of single-layer films.

The fabrication process of multi-layered polymer PCLC films is shown in Fig. 20. Mixtures of two aromatic polyester liquid crystalline polymers (Nippon Oil Corporation; currently, JX Nippon Oil & Energy Corporation) are used to make PCLCs. One of the polymers (chiral polymer) contains 25% chiral units in its chemical composition and the other contains no chiral unit. By changing the ratio of the amounts of the two polymers, the helical pitch of PCLC (photonic band gap wavelength) is controlled.

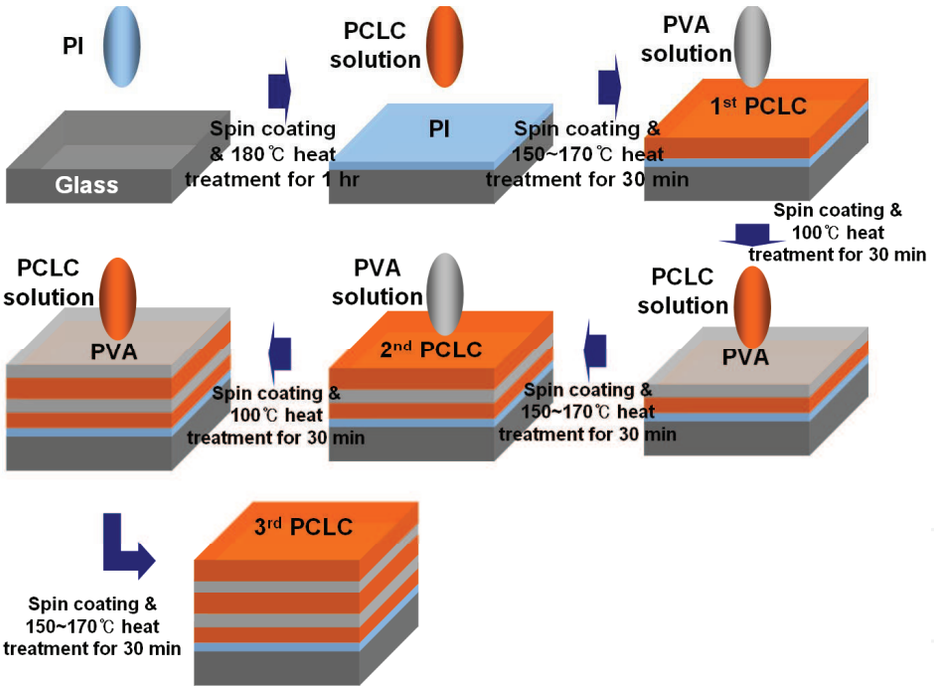

Figure 20. Fabrication process of multi-layered PCLC films.

For fabricating three-layered PCLC films for use as a wide band reflector, the PCLC (λ_p=610 nm; chiral polymer 72 wt%) is spin-cast on glass substrates with unidirectionally rubbed polyimide (PI ; AL1256, JSR). Then, aqueous solution of polyvinyl alcohol (PVA) is spin-cast and the film surface is rubbed again unidirectionally. Another PCLC (λ_p= 510 nm; chrial polymer 87 wt%) is spin-cast on the rubbed PVA surface. The same procedure is repeated for preparing the third PCLC film (λ_p= 530 nm; chrial polymer 82 wt%). Finally PCLC films thus fabricated are cured for 30 min at 160 °C.

The fabrication method of a tunable phase retarder is as follows. The single-layered PCLC films are fabricated by spin coating the solution onto ITO glass substrates coated with PI rubbed unidirectionally at room temperature. The coated PCLC films are cured for 30 min at a temperature over 160 °C in a bake oven, and then quenched to room temperature. The sample cell is made of L-PCLC and PI coated glass substrates and is sustained by spacer. The NLC (ZLI2293, Merck) is introduced into an empty cell using capillary action. The illustration of the fabrication of the final cell is shown in Fig. 21

The OLED structure used here is fabricated in the same way as described in section 2.2. The vacuum evaporated OLEDs with structure of ITO/CuPc/TPD/Alq_3/LiF/Al are described in section 3.2, an spin-coated OLEDs with structure of ITO/PEDOT:PSS/MEH-CN-PPV/LiF/Al are given in section 3.3.

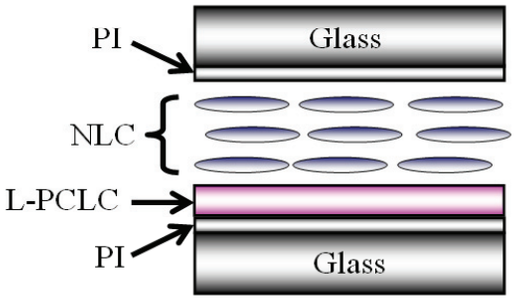

Figure 21. Schematic illustration of tunable phase retarder.[63] Copyright 2008, American Institute of Physics.

3.2. Highly circularly polarized electroluminescence

The device configuration for highly CP-EL from OLEDs is illustrated in Fig. 22. We have simply attached an L-PCLC reflector to an OLED device. After generating the unpolarized light by electrical pumping, the R-CP-EL transmits through the PCLC reflector, whereas L-CP-EL is reflected by the selective reflection of the L-PCLC. This reflected light by the PCLC is still L-CP and changes the polarization to R-CP by getting reflected at the metal surface, and gets transmitted trough the L- PCLC reflector. Thus all the transmitted light has the same sense of rotation, R-CP.

In comparison with the previous work [58] here the band width of the reflector is wider. For fabricating a wide-band CLC reflector, the use of PCLCs has two advantages compared with general low-molecular-weight CLCs. First advantage is that PCLCs used here have higher optical anisotropy (n_e-n_o=0.22), resulting in a wider photonic band gap (PBG). The second advantage is that PCLC films can be easily stacked to multi-layered films by spin-casting. Using these technical advantages we have fabricated a wide-band PCLC reflector using multi-layered PCLC films with different selective reflection bands.

The structure of a three-layered PCLC film with a wide stopband width is shown in Fig. 23(a). The fabrication method of multi-layered PCLC films is already explained in section 3.1. Figure 23(b) shows the reflectance spectra of single-layered and three-layered PCLC

films and the emission spectrum of the active EL material, Alq_3 (see below). A wider selective reflection band formed due to the overlap of the selective reflection bands of the three-layered PCLC films extends to the whole emission band, although the selective reflection band of the single-layered PCLC film covers only the emission peak region.

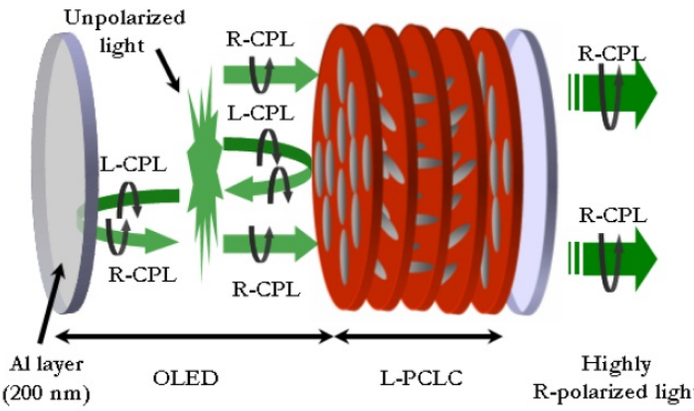

Figure 22. Schematic illustration of a 'photon recycling' device.[62] Copyright 2007, American Institute of Physics.

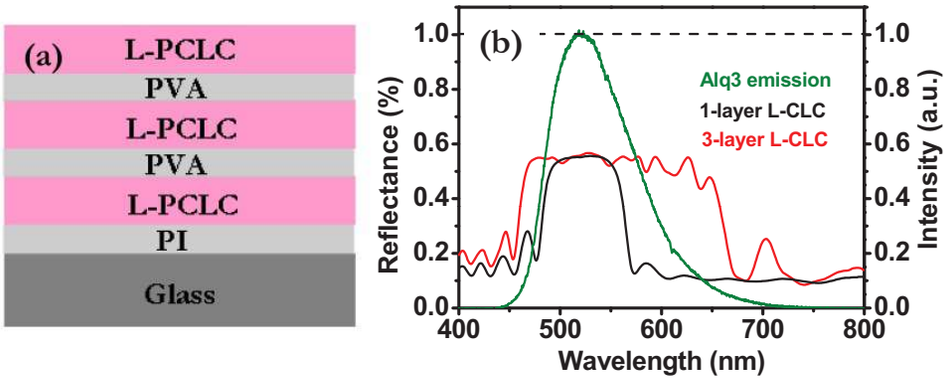

Figure 23. (a) The structure of a three-layered PCLC film. (b) Normalized electroluminescence spectrum of Alq_3 and reflectance spectra of single-layered and three-layered PCLC films.[62] Copyright 2007, American Institute of Physics.

To evaluate the degree of circular polarization quantitatively, R-polarizer and L-polarizer are inserted between the EL device and detector. We confirmed that R- and L-polarized EL intensities are almost the same in OLEDs without a PCLC reflector. In contrast, OLEDs with narrow (single-layered)-PCLC and with wide (three-layered)-PCLC reflectors emit high intensity R-circularly polarized EL within the stopband of PCLC as shown in Fig. 24(a) and 24(b). The R- and L-CP-EL spectra from OLEDs with the narrow-PCLC film are almost the same as that with the wide-PCLC film in the selective reflection region of narrow-PCLC (480nm–560nm) as a result of 'photon recycling'. Outside of the stopband of narrow-PCLC, however, both R- and L-CP components from the narrow-PCLC device do not show any prior circularly polarization characteristics due to the lack of 'photon recycling' (Fig. 24(a)), whereas the wide-PCLC device shows the highly R-circularly polarized light over the whole emission spectrum range, as shown in Fig. 24(b).

It is also noted that the degree of circular polarization is high in the wide-PCLC device over the whole emission band. Figure 25 shows the wavelength dependence of the g-factor [eq. (14)] for light emitted from each device. At the center of the stopband, $|g(\lambda)|$ approaches to 1.67 in both the devices with PCLC films. However, the difference is that $|g(\lambda)|$ remains same over the whole emission band in the wide-PCLC device but it suddenly decreases outside of the stopband in the narrow-PCLC device.

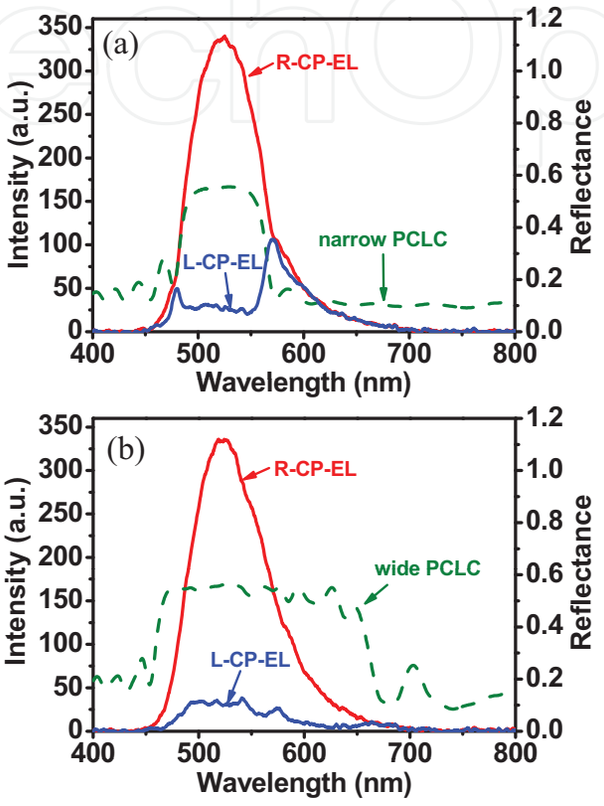

Figure 24. R- and L-CP-EL spectra from OLED devices with (a) narrow- and (b) wide-PCLC films. Reflection spectra for the narrow- and wide-PCLC films are also shown using dotted curves.[62] Copyright 2007, American Institute of Physics.

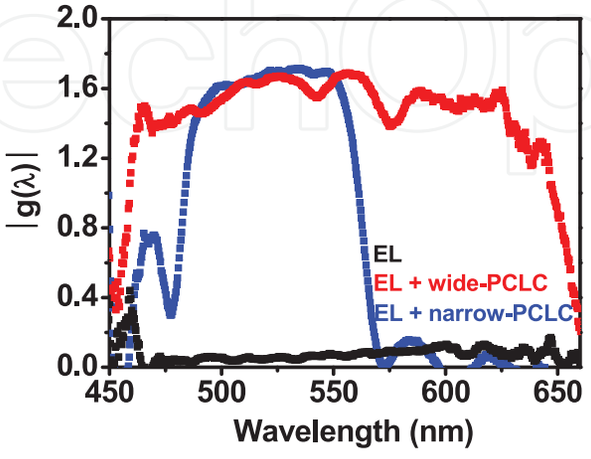

Figure 25. Calculated g-factor values in each device over the whole wavelength range of the emission band of Alq_3.[62] Copyright 2007, American Institute of Physics.

3.3. Polarization-tunable organic light-emitting diodes

In this section, we examine the electro-tunable polarization of electroluminescence by combination of circularly polarized OLEDs (same concept as explained in section 3.2) and tunable phase retarder. A voltage controllable liquid crystal cell is adopted as a tunable phase retarder for tunable polarization characteristics.

The device configuration for polarization-tunable OLEDs with a phase retarder is shown in Fig. 26. For the phase retardation, NLC is filled between the glass substrates with a rubbed PI layer. The phase retarder is simply attached to one of the glass sides of OLEDs. After the generation of unpolarized light from OLED, the whole EL light is extracted as R-CPL by photon recycling. This R-CP-EL can be transformed into arbitrary polarizations by changing the orientation of NLC through applying a voltage. The phase retardation $\Delta\varphi$ at a wavelength λ can be expressed by:

$$\Delta\varphi = \frac{2\pi}{\lambda} d\Delta n \tag{15}$$

where d is cell thickness and Δn is birefringence of NLC.

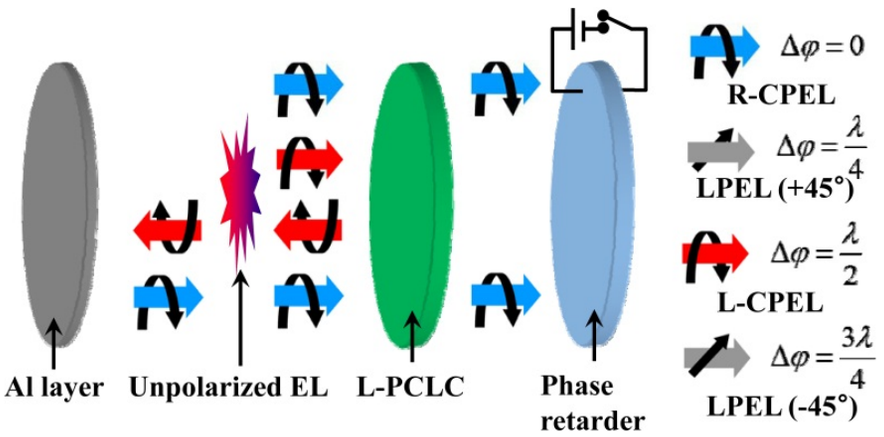

Figure 26. Schematic illustration of the principle of polarization-tunable OLED and polarized light with different polarization.[63] Copyright 2008, American Institute of Physics.

If the wavelength and cell thickness are constant, phase retardation between *e*- and *o*-waves can be varied by applying an electric field. Then the effective birefringence of NLC $\Delta n(\theta)$ is determined by the angle between the director and the substrate surface; i.e., $\Delta n(\theta=0°) = \Delta n$ and $\Delta n(\theta=90°)=0$. If $d\Delta n(\theta)$ is equal to $(2m+1)\lambda/2$ (m = 0, 1, 2…), NLC layer acts as a half-wave plate. On the other hand, if $d\Delta n(\theta)$ is equal to $(4m+1)\lambda/4$ (m = 0, 1, 2…), the NLC layer acts as a quarter wave plate. It should be noted, however, that the maximum phase retardation must be over half-wavelength ($\lambda/2$) to realize four kinds of different polarizations. Hence we have fabricated a cell with the thickness satisfying $3\lambda/2$ retardation condition in the absence of a field.

Figure 27 shows the voltage dependence of transmittance spectra through R-, L- circular and linear polarizers with the direction of +45° and -45°. The applied voltages of 0, 4.5, 6 and 7.5

V correspond to 3λ/2, 5λ/4, λ, 3λ/4 wave plates, respectively. When the R-polarizer is inserted, the spectrum shows a selective reflection band at 0 V (=3λ/2) as shown in Fig. 27(a). This is because the transmitted R-CPL changes its polarization to L-CPL through L-PCLC, and the transmittance decreases down to 0.15 within the selective reflection band. As the voltage increases up to 6 V (=λ), the spectral shape shows no selective reflection band because the phase retarder acts as a full-wave plate. On the other hand, the situation is reversed in L-polarizer as shown in Fig. 27(b).

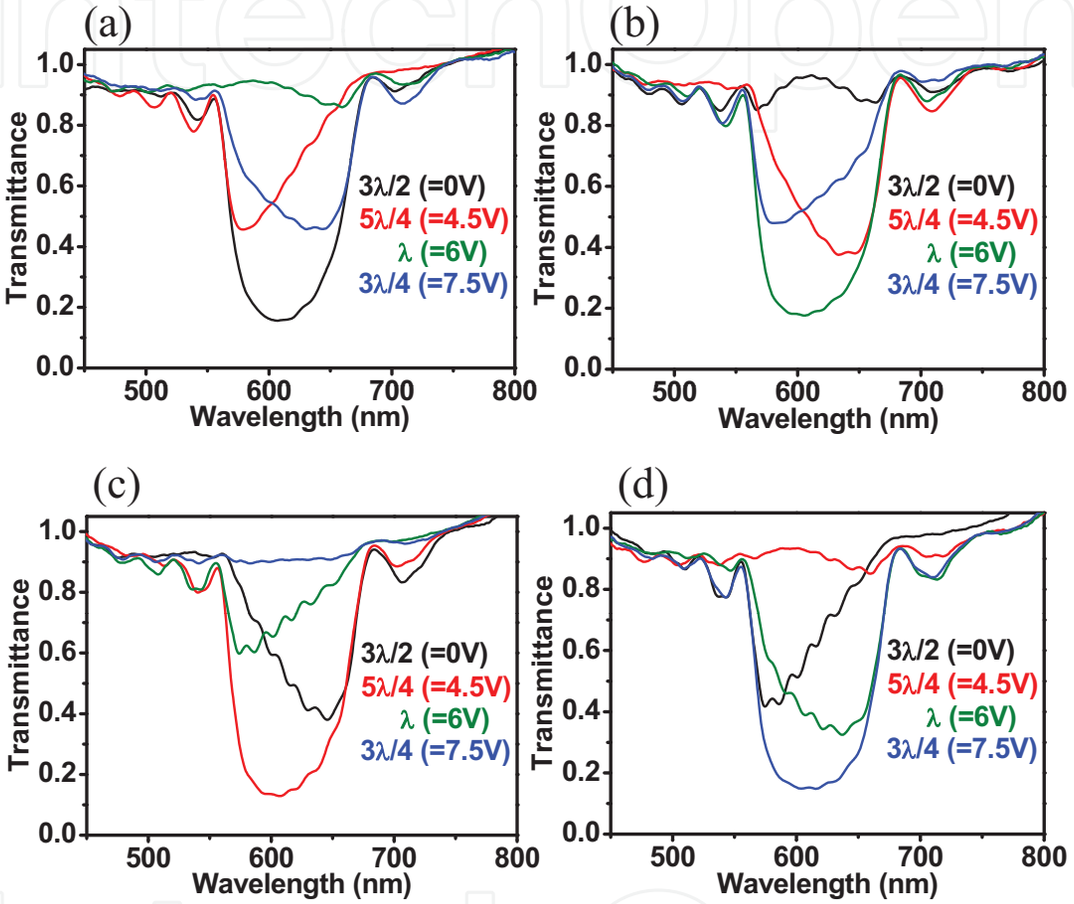

Figure 27. Polarization characteristics of voltage dependent transmittance spectra of a phase retarder. Transmittance spectra of (a) R-CPL, (b) L-CPL, (c) LPL(+45°) and (d) LPL(-45°) under fields of 0, 6, 4.5 and 7.5 V, respectively.[63] Copyright 2008, American Institute of Physics.

Conversion to linearly polarized light is also possible by 4.5 (=5λ/4) and 7.5 V (=3λ/4) applications. If the phase retardation is a quarter-wave, R-CPL changes the polarization condition to linearly-polarized light (LPL). Figure 27(c) and (d) shows LPL with electric field direction of +45° and -45°, respectively. At 4.5 V, the phase retardation is 5λ/4 resulting in a LPL (+45°) as shown in Fig. 27(c). The transmitted R-CPL changes into LPL (-45°) and shows a selective reflection band when the direction of linear polarizer is +45°. On the other hand, if the phase retardation is 3λ/4 (=7.5 V), the transmitted R-CPL changes into LPL (+45°) after transmitted through the linear polarizer. As a result, no selective reflection is observed in the transmittance spectrum. Reversed situation is also observed when the direction of linear polarizer is -45°, as shown in Fig. 27(d).

In order to apply this concept to OLEDs, we have attached a phase retarder to an EL device. This situation is different from the transmittance measurement system because here the EL device has a metallic mirror as a cathode. The output of EL light is R-CP-EL, as explained in Fig. 26. Hence different polarization states are also possible by controlling the birefringence of the NLC layer. To evaluate the degree of polarization quantitatively, R-, L-circular or linear polarizer with the direction of +45° and -45° is inserted in the emissive EL devices between the phase retarder and detector. The output of EL light transmitted from the L-PCLC is R-CP-EL within the wavelength range corresponding to the stopband. The emitted R-CP-EL can be changed into a different polarization by the phase retardation. Figure 28 shows the polarized EL spectra with different polarizations as applied voltage increases from 0 (Fig. 28(a)) to 4.5 (Fig. 28(c)), 6 (Fig. 28(b)), and 7.5 V (Fig. 28(d)). Thus EL light with different polarizations can be selectively emitted by varying the voltage. Outside of the stopband of PCLC, the intensity of opposite polarized light becomes higher because the stopband of PCLC cannot cover a wide wavelength range. It should be noted, however, if a multilayered-PCLC with different pitches is used, the polarization rate can be high over all wavelength [62,67].

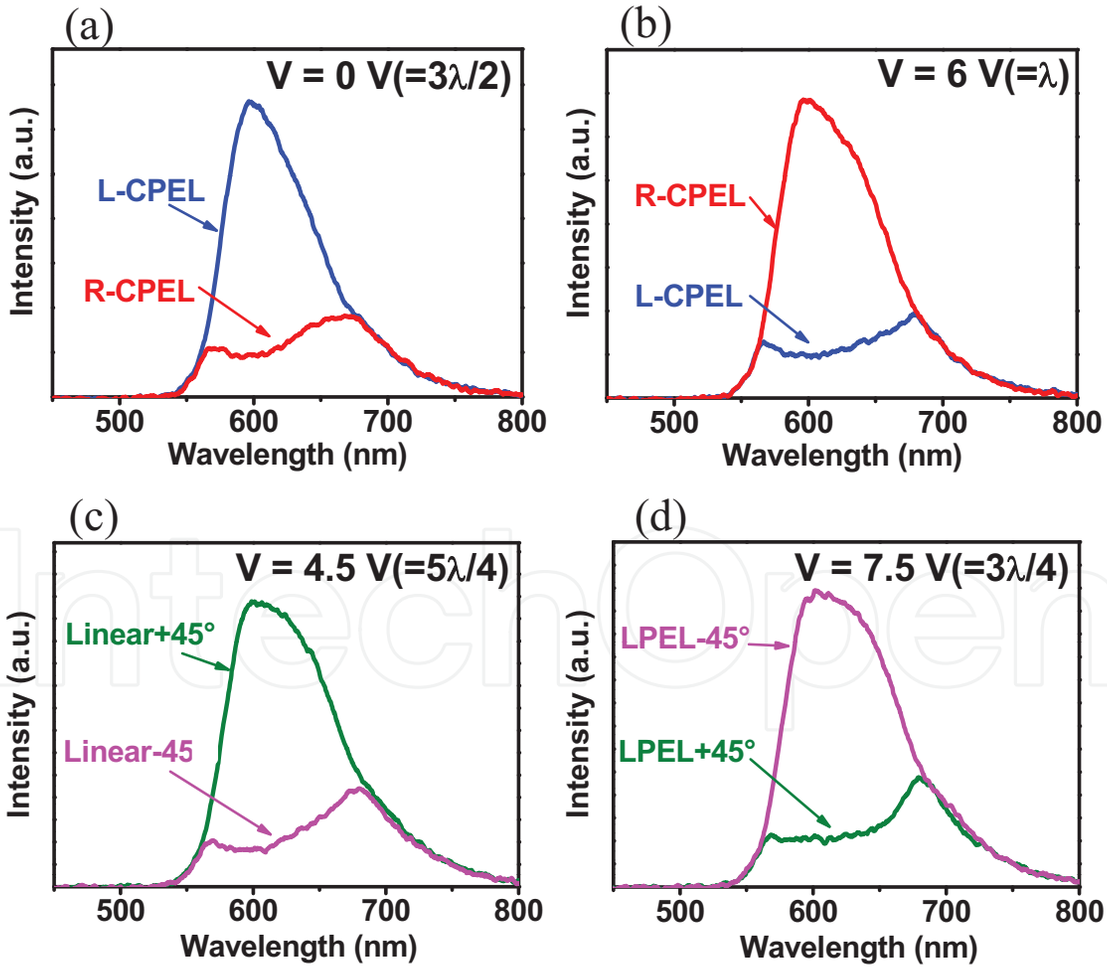

Figure 28. Measured polarized electroluminescence from OLED. Selectively emitted light of (a) L-CP-EL, (b) R-CP-EL, (c) LP-EL(+45°) and (d) LP-EL(-45°) under fields of 0, 6, 4.5, and 7.5 V, respectively.[63] Copyright 2008, American Institute of Physics.

3.4. Polarization conversion in surface-plasmon-coupled emission from corrugated OLEDs with buckling structures

The fabrication process of buckling and OLED devices is almost the same as described in section 2.2. The only difference is the use of a thinner ITO (40 nm) than previous one (120 nm) to extract TM mode preferentially by a surface plasmon coupled emission [68].

To characterize the outcoupled SP mode by buckles, we have calculated its in-plane propagation vectors and plotted the grating period for the emission angles of 0°, 20°, 40°, and 60° as a function of the wavelength of the outcoupled light in Fig. 29(a). Considering the distribution maximum of the buckling periodicity at ~410 nm, it is reasonable that the main diffraction of the SP mode for the normal direction occurs at the emission wavelength of ~690 nm. In addition the FWHM of the periodicity distribution from 300–600 nm allows outcoupling of the SP mode over the entire emission wavelengths by the first- and second-order diffractions. As the emission angle increases, the main diffraction wavelength shifts from ~690 nm for 0° to ~580 nm, ~490 nm, and ~440 nm for 20° , 40° , and 60° , respectively.

We have measured the linearly polarized electroluminescence spectra of the devices with and without buckles at the emission angles of 0°, 20°, 40°, and 60°, and then calculated the light-enhancement ratio (the intensity ratio of the two spectra in the devices with and without buckles) as a function of emission wavelength. Figure 29(b) presents the enhancement ratio of the TM-polarized light. The broad peak intensities for each emission angle are consistent with the main diffraction wavelengths calculated in Fig. 29(a), as indicated by arrows. It is very interesting to note that the TE-polarized light also gets enhanced by buckles as shown in Fig. 29(c). This enhancement is even greater than that for TM-polarized light, particularly at larger emission angles, although generally the SP mode is considered to be excited only by TM-polarized light and the diffraction gratings do not convert the polarization state of an incident light upon diffraction. However, it is also known that the polarization conversion can occur if the grating wavevector is not parallel to the plane of incidence [69-73]. So-called conical diffraction occurs at 0°–90° azimuthal angles by the grating with different wavevectors with respect to the incidence plane, where even TE-polarized light may excite the SP mode because of the existence of the electric field component parallel to the grating vector. In other words, the SP mode excited by a TM-polarized light can be outcoupled to the TE- as well as TM-modes radiation. As the azimuthal angle increases from 0° to 90°, the outcoupled TM mode decreases and the outcoupled TE mode increases by the conical diffractions [69,70]. As far as we know, this was the first report on the polarization state of the extracted SP mode, although a qualitative description on the polarization state can be found for the outcoupled SP mode from a silver cathode with a 2-D corrugated structure [74].

Because the grating vectors in a buckling structure are random over all azimuthal angles, the SP mode in the device with buckles also experiences conical diffractions at all azimuthal angles and then the polarization conversion of the outcoupled light occurs. For example, $k_0 \sin\theta$, k_{SP}, and k_G for the emission wavelength at 600 nm are graphically presented in Fig. 30. Here only one grating wavevector from a 1-D grating with a periodicity of 410 nm is assumed. The radius of the solid circle (blue) corresponds to k_{SP}, the momentum space

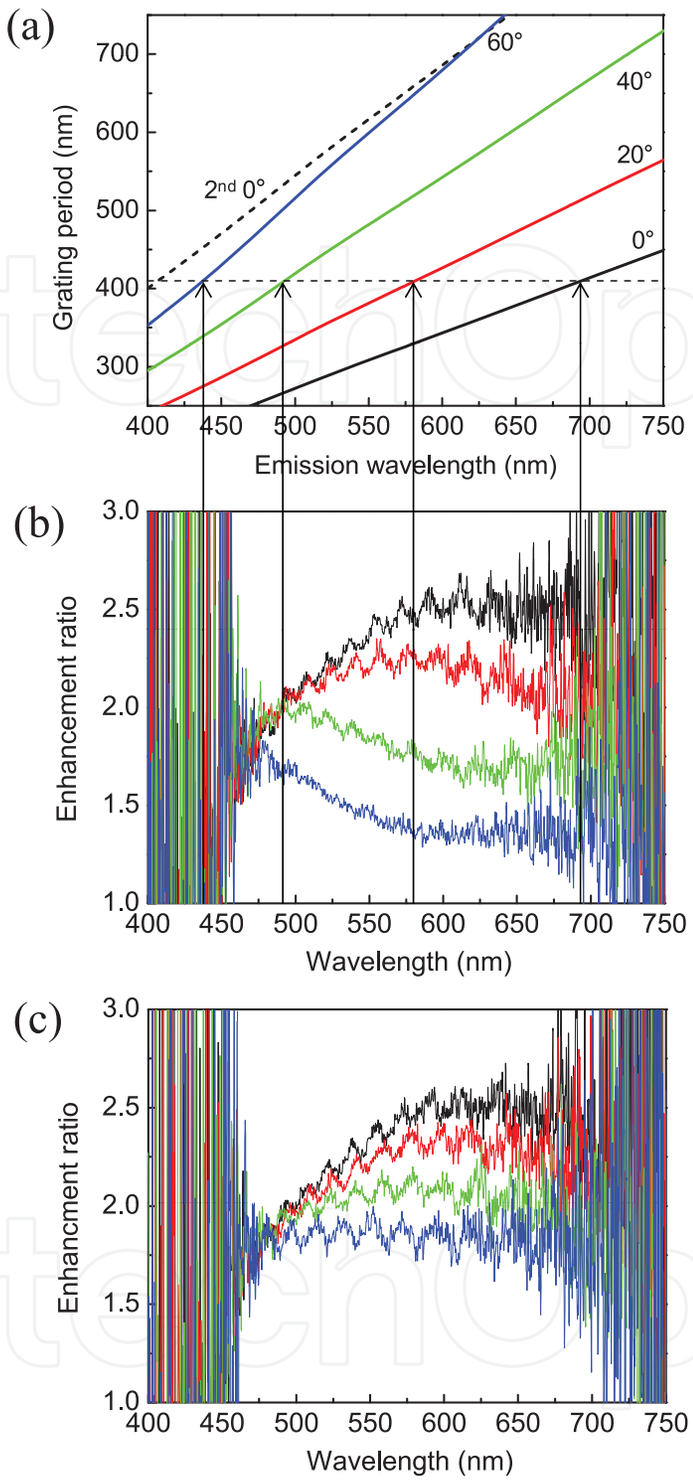

Figure 29. (a) Relation between the outcoupled emission wavelength and the grating period for the emission angles of 0° (black), 20° (red), 40° (green), and 60° (blue), satisfying the first- and second-order (only for 0°) diffractions condition. The dashed horizontal line represents the peak wavelength of 410 nm in the periodicity of the buckles used as the grating. (b) Enhancement ratios of TM-polarized light by buckles at the same angles as (a), 0° (black), 20° (red), 40° (green), and 60° (blue) from top to bottom, obtained by dividing the spectrum (measured through a polarizer) of the device with buckles by that without buckles. (c) Enhancement ratios of TE-polarized light by buckles with the same information as (b). [68] Copyright 2011, Wiley-VCH.

within the solid circle (black) represents the escape zone to air mode, and that between the dotted and solid circle (black) indicates the glass mode. As the azimuthal angle of the SP vector increases, the polar and azimuthal angles of the outcoupled light increase and simultaneously the polarization conversion to the TE mode becomes strong. At an angle of 35°, below the azimuthal angle, the SP mode is outcoupled to the air mode by the grating, between 35°–55° it is trapped to the glass substrate, and above 55° it propagates into the ITO/organic layer with the highly TE-converted polarization. In such a restricted condition of a one-directional grating with a definite periodicity, this ITO/organic mode does not outcouple. However, a conical diffraction to air is expected to occur in our buckling structure over all the possible azimuthal angles, 0–360° because of the grating wavevector distributed over all azimuthal directions. Therefore, the enhancement of the TE-polarized light is observed as shown in Fig. 29(c). However, the greater enhancement of the TE-polarized light than that of the TM-polarized light for all polar angles indicates that more TE-polarized light must be outcoupled to the air mode through the diffraction by buckles, because of the polarization conversion to the TE mode being weak at low azimuthal angles below 35°. Considering the dimension of the emitting area (3 mm × 3 mm) and glass thickness (1.0 mm), most light propagating to the glass substrate cannot undergo reflection or scattering at the corrugated Al layer. Hence the scattering of the glass mode by buckles can be ignored. We believe that the TE-converted light propagating to the ITO/organic layer by the diffraction at an azimuthal angle above 55° can be coupled to the TE_0 leaky guided mode [75], which can then be outcoupled again by the diffraction through the grating vectors with different directions. The broad periodicity and random orientation of buckles contribute to the additional extraction of the TE-polarized light for all polar angles, thereby producing a higher enhancement of the TE-polarized light over all polar angles.

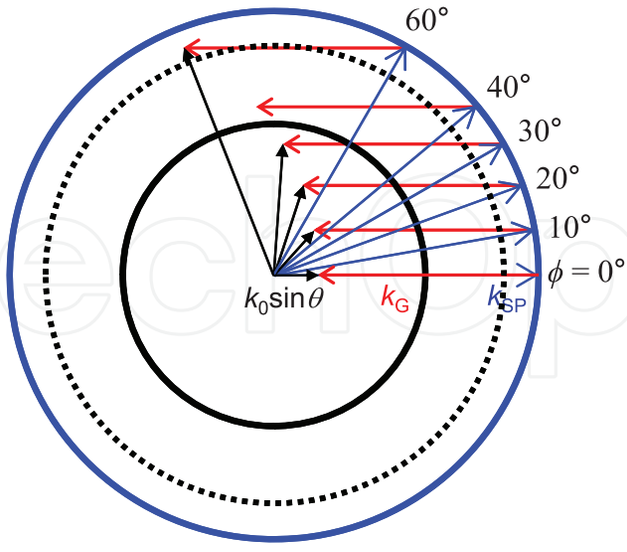

Figure 30. Momentum representations of SP mode (blue circle, k_{SP}), glass light-line (black dotted circle), air light-line (black solid line), grating wave vector (red arrow, k_G), and the outcoupled light to air mode (black arrow, $k_0 \sin\theta$) for the emission wavelength of 600 nm. θ and ϕ represent the polar and azimuthal angle, respectively. Only one-directional grating vector from one-dimensional grating with a periodicity of 410 nm is assumed. [68] Copyright 2011, Wiley-VCH.

To confirm the polarization conversion by buckles on diffraction, a buckled resin layer on a glass substrate, coated with a 100-nm-thick Al layer, is irradiated using a linearly polarized He–Ne laser (632.8 nm) at an incident angle of 60° and the scattered light from the surface normal observed through a linear polarizer. We have found that the incident TM-polarized light is largely converted into the TE mode upon diffraction. The ratio of TE- to TM-polarized light intensities was around 0.7, irrespective of the incident azimuthal angle. This result is consistent with the enhancement of the TE-polarized light by buckles in the device structure shown in Fig. 29(c).

4. Summary

After summarizing methods for enhanced outcoupling in OLED devices, we reviewed enhancement methods using photonic structures at a surface. As explained in sections 2.3 and 2.4, corrugated EL devices with periodic or quasi-periodic nanostructures show enhanced light extraction performance compared with the reference flat device without such structures. The principle of light extraction is the same in both device configurations; however, periodically corrugated EL device shows higher light extraction only at a specific wavelength because of the well-defined corrugation pitch. This anisotropic angular dependence does not satisfy the Lambertian emission pattern, which is an important requirement in the lighting technologies. On the other hand, spontaneously formed buckling patterns on OLEDs towards air are effectively used as a quasi-periodic structure to extract light from the waveguide modes. The characteristics of the broad periodicity distribution and randomly oriented wave vectors of buckles provide an invaluable advantage of possible outcoupling of the waveguide light propagating along any direction with a wide spectral range. Namely a buckling device shows a Lambertian emission pattern with an increase in emission angle, which satisfies the requirement of OLED lighting. In particular, it enhances the outcoupling of waveguide modes at various wavelength ranges due to the broad distribution of the periodicity that can be applied to white OLEDs. We may conclude that the buckling device structure overcomes the limitation of periodic nanostructures and it can be used in the development of white OLEDs for lighting.

We have also demonstrated the generation of highly circularly polarized EL and its tunability using a liquid crystal phase retarder. A wide-band reflector has enabled us to obtain high ratio of brightness between R-CP-EL and L-CP-EL with the overall intensity ratio of about 10 and *g*-factor of about 1.6 over the whole emission band. Also, using a voltage dependent phase retarder, we have confirmed that there is no limitation for choosing emissive materials to obtain the tunable polarized EL light. We have also shown that the devices with buckles have double current and power efficiencies over the entire emission wavelengths and emission angles. This is achieved without any spectral changes even though ITO thickness is thin (40 nm) to outcouple the only SP (TM) mode which would otherwise be lost into the Al cathode layer of OLED devices. It is also found that the diffraction of the SP mode by buckles causes polarization conversion to the TE mode with a higher light intensity than in the TM mode, which occurs due to the random orientation of the buckling structure.

Author details

Soon Moon Jeong
Nano and Bio Research Division, Daegu Gyeongbuk Institute of Science and Technology, Sang-Ri, Hyeonpung-Myeon, Dalseong-Gun, Daegu, Republic of Korea

Hideo Takezoe*
Department of Organic and Polymeric Materials, Tokyo Institute of Technology, O-okayama, Meguro-ku, Tokyo, Japan

5. References

[1] Adachi. C, Baldo M. A, Thompson M. E, Forrest S. R. Nearly 100% Internal Phosphorescence Efficiency in an Organic Light-emitting Device. J. Appl. Phys. 2011;90: 5048-5051.

[2] Benisty H, Neve H. D, Weisbuch C. Impact of Planar Microcavity Effects on Light Extraction - Part I: Basic Concepts and Analytical Trends. IEEE J. Quantum Electron. 1998;34: 1612-1631.

[3] Benisty H, Neve H. D, Weisbuch C. Impact of Planar Microcavity Effects on Light Extraction - Part II: Selected Exact Simulations and Role of Photon Recycling. IEEE J. Quantum Electron. 1998;34: 1632-1643.

[4] Meerholz K, Muller D. C. Outsmarting Waveguide Losses in Thin-Film Light-Emitting Diodes. Adv. Funct. Mater. 2001;11: 251-253.

[5] Tsutsui T, Yahiro M, Yokogawa H, Kawano K, Yokoyama M. Doubling Coupling-Out Efficiency in Organic Light-Emitting Devices Using a Thin Silica Aerogel Layer. Adv. Mater. 2001;13: 1149-1152.

[6] Madigan C. F, Lu M. H, Sturm J. C. Improvement of Output Coupling Efficiency of Organic Light-emitting Diodes by Backside Substrate Modification. Appl. Phys. Lett. 2000;451: 1650-1652.

[7] A Chutinan, Ishihara K, Asano T, Fujita M, Noda S. Theoretical Analysis on Light-extraction Efficiency of Organic Light-emitting Diodes Using FDTD and Mode-expansion Methods. Org. Electronics. 2005;6: 3-9.

[8] Gu. G, Garbuzov D. Z, Burrows P. E, Venkatesh S, Forrest S. R, Thompson M. E. High-external-quantum Efficiency Organic Light-emitting Devices. Opt. Lett. 1997;22: 396-398.

[9] Greenham N. C, Friend R. H, Bradley D. D. C. Angular Dependence of the Emission from a Conjugated Polymer Light-Emitting Diode: Implications for Efficiency Calculations. Adv. Mater. 1994;6: 491-494.

[10] Windisch R., Heremans P., Knobloch A., Kiesel P., Dohler G. H., Dutta B., Borghs G. Light-emitting Diodes with 31% External Quantum Efficiency by Outcoupling of Lateral Waveguide Modes. Appl. Phys. Lett. 1999;74: 2256-2258.

* Corresponding Author

[11] Moller S, Forrest S. R. Improved Light Out-coupling in Organic Light Emitting Diodes Employing Ordered Microlens Arrays. J. Appl. Phys. 2002:91; 3324-3327.
[12] Sun J, Forrest S. R. Organic Light Emitting Devices with Enhanced Outcoupling via Microlenses Fabricated by Imprint Lithography. J. Appl. Phys. 2006;100: 073106.
[13] Yamasaki T., Sumioka K., and Tsutsui T. Organic Light-emitting Device with an Ordered Monolayer of Silica Microspheres as a Scattering Medium. Appl. Phys. Lett. 2000;76: 1243-1245.
[14] Jordan R. H., Rothberg L. J., Dodabalapur A., and Slusher R. E. Efficiency Enhancement of Microcavity Organic Light Emitting Diodes. Appl. Phys. Lett. 1996;69: 1997-1999.
[15] Dirr S, Wiese S, Johannes H, Kowalsky W. Organic Electro- and Photoluminescent Microcavity Devices. Adv. Mater. 1998;10: 167-171.
[16] Han S, Huang C, Lu Z. Color Tunable Metal-cavity Organic Light-emitting Diodes with Fullerene Layer. J. Appl. Phys. 2005;97: 093102.
[17] Lemmer U., Hennig R., Guss W., Ochse A., Pommerehne J., Sander R., Greiner A., Mahrt R. F., Bassler H., Feldmann J., Gobel E. O. Microcavity Effects in a Spin-coated Polymer Two-layer System. Appl. Phys. Lett. 1995;66: 1301-1303.
[18] Dodabalapur A., Rothberg L. J., Miller T. M., and Kwock E. W. Microcavity Effects in Organic Semiconductors. Appl. Phys. Lett. 1994;64: 2486-2488.
[19] Dodabalapur A, Rothberg L. J, Jordan R. H, Miller T. M, Slusher R. E, Phillips J. M. Physics and Applications of Organic Microcavity Light Emitting Diodes. J. Appl. Phys. 1996;80: 6954-6964.
[20] Tsutsui T., Takada N., Saito S., Ogino E. Appl. Phys. Lett. Sharply Directed Emission in Organic Electroluminescent Diodes with an Optical-microcavity Structure. 1994;65: 1868-1870.
[21] Matterson B. J, Matterson J, Lupton J. M, Safonov A. F, Salt M. G, Barnes W. L, Samuel I. D. W. Increased Efficiency and Controlled Light Output from a Microstructured Light-emitting Diode. Adv. Mater. 2001;13: 123-127.
[22] Lupton J. M., Matterson B. J., Samuel I. D. W., Jory M. J., Barnes W. L. Bragg Scattering from Periodically Microstructured Light Emitting Diodes. Appl. Phys. Lett. 2000;77: 3340-3342.
[23] Ziebarth J. M, Saafir A. K, Fan S, McGehee M. D. Extracting Light from Polymer Light-Emitting Diodes Using Stamped Bragg Gratings. Adv. Funct. Mater. 2004;14: 451-456.
[24] Ziebarth J. M, McGehee M. D. A Theoretical and Experimental Investigation of Light Extraction from Polymer Light-emitting Diodes. J. Appl. Phys. 2005;97: 064502.
[25] Hobson P. A, Wasey J. A. E, Sage I, Barnes W. L. The Role of Surface Plasmons in Organic Light-emitting Diodes. IEEE J. Sel. Top. Quantum Electron. 2002;8: 378-386.
[26] Ishihara K, Fujita M, Matsubara I, Asano T, Noda S, Ohata H, Hirasawa A. Nakada H., Shimoji N. Organic Light-emitting Diodes with Photonic Crystals on Glass Substrate Fabricated by Nanoimprint Lithography. Appl. Phys. Lett. 2007;90: 111114.
[27] Fujita M., Ueno T., Ishihara K., Asano T., Noda S., Ohata H., Tsuji T., Nakada H., and Shimoji N. Reduction of Operating Voltage in Organic Light-emitting Diode by Corrugated Photonic Crystal Structure. Appl. Phys. Lett. 2004;85: 5769-5771.

[28] Fujita M, Ishihara K, Ueno T, Asano T, Noda S, Ohata H, Tsuji T, Nakada H, Shimoji N. Optical and Electrical Characteristics of Organic Light-Emitting Diodes with Two-Dimensional Photonic Crystals in Organic/Electrode Layers. Jpn. J. Appl. Phys. 2005;44: 3669-3677.

[29] Schnitzer I., Yablonovitch E., Caneau C., Gmitter T. J., Scherer A. 30% External Quantum Efficiency from Surface Textured, Thin-film Light-emitting Diodes. Appl. Phys. Lett. 1993;63: 2174-2176.

[30] Lim J, Oh S. S, Kim D. Y, Cho S. H, Kim I. T, Han S. H, Takezoe H. Enhanced Out-coupling Factor of Microcavity Organic Light-emitting Devices with Irregular Microlens Array. Opt. Express 2006;14: 6564-6571.

[31] Schubert E. F., Wang Y. H., Cho A. Y., Tu L. W., Zydzik G. J. Resonant Cavity Light-emitting Diode. Appl. Phys. Lett. 1992;60: 921-923.

[32] Hunt N. E. J., Schubert E. F., Logan R. A., Zydzik G. J. Enhanced Spectral Power Density and Reduced Linewidth at 1.3 μm in an InGaAsP Quantum Well Resonant-cavity Light-emitting Diode. Appl. Phys. Lett. 1992;61: 2287-2289.

[33] Jeong S. M., Araoka F., Machida Y., Ishikawa K., Takezoe H., Nishimura S., Suzaki G. Enhancement of Normally Directed Light Outcoupling from Organic Light-emitting Diodes Using Nanoimprinted Low-refractive-index Layer. Appl. Phys. Lett. 2008;92: 083307.

[34] Jeong S. M., Ha N. Y., Araoka F., Ishikawa K., Takezoe H. Electrotunable Polarization of Surface-emitting Distributed Feedback Laser with Nematic Liquid Crystals. Appl. Phys. Lett. 2008;92: 171105.

[35] Jeong S. M, Araoka F, Machida Y, Takanishi Y, Ishikawa K, Takezoe H, Nishimura S, Suzaki G. Enhancement of Light Extraction from Organic Light-emitting Diodes with Two-Dimensional Hexagonally Nanoimprinted Periodic Structures Using Sequential Surface Relief Grating. Jpn. J Appl. Phys. 2008;47: 4566-4571.

[36] Koo W. H, Jeong S. M, Araoka F, Ishikawa K, Nishimura S, Toyooka T, Takezoe H. Light Extraction from Organic Light-emitting Diodes Enhanced by Spontaneously Formed Buckles. Nat. Photonics 2010;4: 222-226.

[37] Hubert C., Debuisschert C. F-., Hassiaoui I., Rocha L., Raimond P., Nunzi J.-M. Emission Properties of an Organic Light-emitting Diode Patterned by a Photoinduced Autostructuration Process. Appl. Phys. Lett. 2005;87: 191105.

[38] Lawrence J. R., Andrew P., Barnes W. L., Buck M., Turnbull G. A., Samuel I. D. W. Optical Properties of a Light-emitting Polymer Directly Patterned by Soft Lithography. Appl. Phys. Lett. 2002;81: 1955-1957.

[39] Jeong S. M, Takanishi Y, Ishikawa K, Nishimura S, Suzaki G, Takezoe H. Sharply Directed Emission in Microcavity Organic Light-emitting Diodes with a Cholesteric Liquid Crystal Film. Opt. Comm. 2007;273: 167-172.

[40] Burrows P. E, Shen Z, Bulovic V, McCarty D. M, Forrest S. R. Relationship Between Electroluminescence and Current Transport in Organic Heterojunction Light-emitting Devices. J. Appl. Phys. 1996;79: 7991-8006.

[41] Kalinowski J., Electroluminescence in organics. J. Phys. D 1999;32: R179-R250.

[42] Hobson P. A, Wedge S, Wasey J. A. E, Sage I, Barnes W. L. Surface Plasmon Mediated Emission from Organic Light-Emitting Diodes. Adv. Mater. 2002;14: 1393-1396.
[43] Bowden N, Brittain S, Evans A. G, Hutchinson J. W, Whitesides G. M. Spontaneous Formation of Ordered Structures in Thin Films of Metals Supported on an Elastomeric Polymer. Nature 1998;393: 146-149.
[44] Okayasu T, Zhang H. L, Bucknall D. G, Briggs G. A. Spontaneous Formation of Ordered Lateral Patterns in Polymer Thin-film Structures. Adv. Func. Mater. 2004;14: 1081-1088.
[45] Huck W. T. S, Bowden N, Onck P, Pardoen T, Hutchinson J. W, Whitesides G. M. Ordering of Spontaneously Formed Buckles on Planar Surfaces. Langmuir 2000;16: 3497-3501.
[46] Allen H. G., Analysis and Design of Structural Sandwich Panels (Pergamon, 1969).
[47] Cerda E, Mahadevan L. Geometry and Physics of Wrinkling. Phys. Rev. Lett. 2003;90: 074302.
[48] Bowden N., Huck W. T. S., Paul K. E., Whitesides G. M. The Controlled Formation of Ordered, Sinusoidal Structures by Plasma Oxidation of an Elastomeric Polymer. Appl. Phys. Lett. 1999;75: 2557-2559.
[49] Kalinowski J, Palilis L. C, Kim W. H, Kafafi Z. H. Determination of the Width of the Carrier Recombination Zone in Organic Light-emitting Diodes. J. Appl. Phys. 2003;94: 7764-7767.
[50] Tang C. W, VanSlyke S. A, Chen C. H. J. Electroluminescence of Doped Organic Thin Films. J. Appl. Phys. 1989;65: 3610-3616.
[51] Mochizuki H, Hasui T, Shiono T, Ikeda T, Adachi C, Taniguchi Y, Shirota Y. Emission Behavior of Molecularly Doped Electroluminescent Device Using Liquid-crystalline Matrix. Appl. Phys. Lett. 2000;77: 1587-1589.
[52] Furumi S, Sakka Y. Chiroptical Properties Induced in Chiral Photonic-Bandgap Liquid Crystals Leading to a Highly Efficient Laser-Feedback Effect. Adv. Mater. 2006;18: 775-780.
[53] O'Neill M, Kelly S. M. Liquid Crystals for Charge Transport, Luminescence, and Photonics. Adv. Mater. 2003;15: 1135-1146.
[54] Grell M, Knoll W, Lupo D, Meisel A, Miteva T, Neher D, Nothofer H, Scherf U, Yasuda A. Blue Polarized Electroluminescence from a Liquid Crystalline Polyfluorene. Adv. Mater. 1999;11: 671-675.
[55] Grell M, Bradley D. D. C. Polarized Luminescence from Oriented Molecular Materials. Adv. Mater. 1999;11: 895-905.
[56] Peeters E, Christians M. P. T, Janssen R.A. J, Schoo H. F. M, Dekkers H. P. J. M, Meijer E. W. Circularly Polarized electroluminescence from a Polymer Light-emitting Diode. J. Am. Chem. Soc. 1997;119: 9909-9910.
[57] Oda M, Nothofer H, Lieser G, Scherf U, Meskers S. C. J, Neher D. Circularly Polarized Electroluminescence from Liquid-Crystalline Chiral Polyfluorenes. Adv. Mater. 2000;12: 362-365.
[58] Grell M., Oda M., Whitehead K. S., Asimakis A, Neher D, Bradley D. D. C. A Compact Device for the Efficient, Electrically Driven Generation of Highly Circularly Polarized Light. Adv. Mater. 2001;13: 577-580.

[59] Belayev S. V., Schadt M., Barnik M. I., Funfschilling J., Malimoneko N. V., Schmitt K., Large Aperture Polarized Light Source and Novel Liquid Crystal Display Operating Modes. Jpn. J. Appl. Phys. 1990;29: L634-L637.

[60] Woon K. L, O'Neill M, Richards G. J, Aldred M. P, Kelly S. M, Fox A. M. Highly Circularly Polarized Photoluminescence over a Broad Spectral Range from a Calamitic, Hole-transporting, Chiral Nematic Glass and from an Indirectly Excited Dye. Adv. Mater. 2003;15: 1555-1558.

[61] Geng Y, Trajkovska A, S. Culligan W, Ou J. J, Chen H. M. P, Katsis D, Chen S. H. Origin of Strong Chiroptical Activities in Films of Nonafluorenes with a Varying Extent of Pendant Chirality. J. Am. Chem. Soc. 2003;125: 14032-14038.

[62] Jeong S. M., Ohtsuka Y., Ha N. Y., Takanishi Y., Ishikawa K., Takezoe H. Highly Circularly Polarized Electroluminescence from Organic Light-emitting Diodes with Wide-band Reflective Polymeric Cholesteric Liquid Crystal Films. Appl. Phys. Lett. 2007;90: 211106.

[63] Jeong S. M, Ha N. Y, Takezoe H, Nishimura S, Suzaki G. Polarization-tunable Electroluminescence Using Phase Retardation Based on Photonic Bandgap Liquid Crystal. J. Appl. Phys. 2008;103: 113101.

[64] Hwang J, Song M. H, Park B, Nishimura S, Toyooka T, Wu J. W, Takanishi Y, Ishikawa K, Takezoe H. Electro-tunable Optical Diode Based on Photonic Bandgap Liquid-crystal Heterojunctions. Nat. Mater. 2005;4: 383-387.

[65] Song M. H, Park B, Nishimura S, Toyooka T, Chung I. J, Takanishi Y, Ishikawa K, Takezoe H. Electrotunable Non-reciprocal Laser Emission from a Liquid-Crystal Photonic Device. Adv. Funct. Mater. 2006;16: 1793-1798.

[66] Song M. H, Park B, Shin K.-C, Ohta T, Tsunoda Y, Hoshi H, Takanishi Y, Ishikawa K, Watanabe J, Nishimura S, Toyooka T, Zhu Z, Swager T. M, Takezoe H. Effect of Phase Retardation on Defect-Mode Lasing in Polymeric Cholesteric Liquid Crystals. Adv. Mater. 2004;16: 779-783.

[67] Broer D. J, Mol G. N. Wide-band Reflective Polarizers from Cholesteric Polymer Networks with a Pitch Gradient. Nature 1995;378: 467-469.

[68] Koo W. H, Jeong S. M, Nishimura S, Araoka F, Ishikawa K, Toyooka T, Takezoe H. Polarization Conversion in Surface-Plasmon-Coupled Emission from Organic Light-Emitting Diodes Using Spontaneously Formed Buckles. Adv. Mater. 2011;23: 1003-1007.

[69] Inagaki T, Motosuga M, Yamamori K. Photo-acoustic Study of Plasmon Resonance-absorption in a Diffraction Grating. Phys. Rev. B. 1983;28: 1740-1744.

[70] Inagaki T, Goudonnet J. P, Arakawa E. T. Plasma Resonance Absorption in Conical Diffraction: Effects of Groove Depth. J. Opt. Soc. Am. B 1986;3: 992-995.

[71] Elston S. J, Bryan-Brown G. P, Sambles J. R. Polarization Conversion from Diffraction Gratings. Phys. Rev. B. 1991;44: 6393-6400.

[72] Bristow A. D., Astratov V. N., Shimada R., Culshaw I. S., Skolnick M. S., Whittaker D. M., Tahraoui A., Krauss T. F., Polarization Conversion in the Reflectivity Properties of Photonic Crystal Waveguides. IEEE J. Quantum. Elect. 2002;38: 880-884.

[73] Suyama T, Okuno Y, Matsuda T. Enhancement of TM-TE mode Conversion Caused by Excitation of Surface Plasmons on a Metal Grating and its Application for Refractive Index Measurement. Prog. Electromagn. Res. 2007;72: 91-103.
[74] Feng J, Okamoto T, Kawata S. Enhancement of Electroluminescence Through a Two-dimensional Corrugated Metal Film by Grating-induced Surface-plasmon Cross Coupling. Opt. Lett. 2005;30: 2302-2304.
[75] Reinke N. A, Ackermann C, Brütting W. Light Extraction via Leaky Modes in Organic Light Emitting Devices. Opt. Commun. 2006;266: 191-197.

IntechOpen